J. Fluid Mech. (2002), *vol.* 471, *pp.* 71–106.
DOI: 10.1017/S0022112002001994 Printed in the United Kingdom

Chaotic dynamics in a strained rotating flow: a precessing plane fluid layer

By R. M. MASON AND R. R. KERSWELL

Department of Mathematics, University of Bristol, Bristol, BS8 1TW, UK

(Received 4 September 2001 and in revised form 13 June 2002)

The nonlinear dynamics exhibited by a planar layer of precessing fluid is examined as a canonical example of a strained rotating flow. The simple basic flow, $\boldsymbol{U}_{basic} = -Y\hat{\boldsymbol{X}} + (X - 2\epsilon Z)\hat{\boldsymbol{Y}}$ in a frame rotating at $\epsilon\hat{\boldsymbol{X}}$, consists of sheared circular streamlines (where ϵ measures the shearing) which are linearly unstable through the pairwise resonance of two inertial waves in a fashion similar to elliptical flow. Direct numerical simulation shows that the weakly nonlinear regime is quickly disrupted by further instabilities which lead to a multitude of co-existing solution branches, some of which represent chaotic flows. All these solutions remain within $O(\epsilon)$ (in an energy norm) of $\boldsymbol{U}_{basic}$ so that energy is not apparently withdrawn from the fluid's underlying rotation. Further increases in the precession rate cause the flow to branch-switch randomly between these now quasi-stable states so that a new form of 'slow' dynamics emerges. The implication of this and the fact that these instabilities can nevertheless be classed as 'strong' is discussed from the perspective of the closely related problem of the precessing Earth and laboratory models thereof.

1. Introduction

Rotating flows are rarely uniform in Nature. Typically, external boundary conditions induce strains on the flow so that the circular fluid streamlines become distorted. These asymmetries can drive strong inertial instabilities which have been observed to lead to turbulent breakdown. One particular example of this phenomenon – 'elliptical' flow – has been studied extensively. The linear instability of elliptical streamlines was discovered simultanously in the contexts of a strained vortex (Moore & Saffman 1975) and a rotating fluid-filled triaxial ellipsoid (Gledzer *et al.* 1974, 1975), and is now well understood (Kerswell 2002); however, efforts to understand the nonlinear evolution of the instability have been hampered by the absence of a natural situation to simulate numerically. The obvious choice of studying elliptical flow in a plane layer is not available unless compromises are made to enforce periodicity (Lungren & Mansour 1996). Dealing with more appropriate open flows (Laporte & Corjon 2000) or elliptical geometries (Mason & Kerswell 1999) has necessarily limited what can be learnt owing to the increased numerical overhead. As a result, many questions still remain about the nonlinear evolution of strained rotating flows beyond the initial instability. The presence of secondary instabilities is now accepted after the corroboration of theory (Kerswell 1999) by numerical simulation (Mason & Kerswell 1999) and experiment (Eloy, Le Gal & Le Dizès 2000, 2002). However, what happens next, given the number of inertial waves present and hence the rich possibilities for further triad resonances, is unclear. The Ruelle–Takens transition scenario (Ruelle & Takens 1971) suggests that transition to a strange attractor (and presumably turbulence) may only be a

further one or two bifurcations away. Certainly, the experiments of Malkus (1989) and Eloy *et al.* (2000, 2002) in which they see a sudden breakdown of the flow to small scales would tend to support this, as would the direct numerical simulations of Lungren & Mansour (1996) who report seeing only a primary and a secondary instability before the flow apparently becomes turbulent. In this paper, we aim to explore this gap between the emergence of a secondary instability and the appearance of small-scale disorder.

Precessing flows offer an alternative arena to elliptical flows in which to study strained rotating fluids. Produced when the axis of a vortex is forced to rotate, a precessing flow is characterized by a strain perpendicular to the plane of the streamlines. In the precessing frame, the streamlines remain circular but now are sheared across each other so that their line of centres is no longer perpendicular to the plane of motion. This is in contrast to elliptical flow where the strain is in the plane of motion and causes the circular streamlines to become elliptical. Despite these differences, instability in each case manifests itself through the pairwise resonance of inertial waves although the details – the resonance conditions for two particular waves to grow – obviously differ (Kerswell 2002). As a result, the nonlinear dynamics for precessing flows should be very similar in character to that for elliptical flow. Studying precessing flows, however, has the considerable advantage that a particularly accessible plane layer model may be formulated. Given this, the main purpose of this paper is to explore the nonlinear dynamics generated by precessional instabilities within such a model using direct numerical simulation. Leading issues to be addressed include determining the form of the bifurcation structure beyond criticality. Although the primary and secondary bifurcations are known to be supercritical, subsequent subcriticality could mean the instability undergoes a sudden transition. This has a bearing on the 'strength' of the instability as measured by how quickly the sustainable disturbance energy grows as a function of the bifurcation parameter. The co-existence of multiple nonlinear states would also be a strong indication of complex temporal behaviour.

Beyond addressing these fundamental issues in strained rotating flows, the other motivation for this study is the renewed interest in understanding the precessional response of the Earth's fluid-filled outer core (Vanyo & Dunn 2000; Lorenzani & Tilgner 2001; Noir, Jault & Cardin 2001; Pais & Le Mouel 2001; Tilgner & Busse 2001). The Earth's outer core is traditionally modelled in the laboratory as a slightly oblate fluid-filled spheroid spinning quickly about its axis of symmetry which is forced to undergo slow retrograde precession (e.g. Malkus 1968; Vanyo 1991; Vanyo *et al.* 1995). Such experiments have revealed a plethora of interesting flows culminating in a fully turbulent response at high enough precession rates (Malkus 1968). Unfortunately, it still remains unclear how to scale up these results to Earthlike parameters. This is because the 'basic' laminar precessional response, which is the viscously corrected version of Poincaré's (1910) famous solution, is a complicated mixture of inertial strains in the interior (Kerswell 1993) and small-scale viscous effects which exist not only at the boundary but throughout the interior in the form of viscous shear layers (Stewartson & Roberts 1963; Roberts & Stewartson 1965; Busse 1968; Hollerbach & Kerswell 1995; Kerswell 1995; Tilgner 1999*a–c*; Noir *et al.* 2001; Tilgner & Busse 2001). Not surprisingly, a complete stability analysis of this three-dimensional small-scale flow within the crucially non-spherical geometry of an oblate spheroid represents a formidable undertaking. A recent attempt at direct numerical simulation has unfortunately been thwarted by weak Ekman boundary-layer instabilities which although not significantly affecting the interior flow do lead to unresolvably small

scales (Lorenzani & Tilgner 2001). Despite this, Lorenzani & Tilgner (2001) were also able to find viscously generated instabilities in the interior, but again, these were weak (the energy in the instability K_{inst} never exceeded 1% of the total energy K of the flow in the precessing rotating frame). A separate effort to examine the stability of the viscous structures by studying a precessing fluid-filled sphere has also found similarly weak viscous instabilities with $O(10^{-4}) \leqslant K_{inst}/K \leqslant O(10^{-2})$ (Tilgner & Busse 2001).

In the absence of viscosity, it can be shown that Poincaré's inviscid solution as a strained rotating flow is linearly unstable to the pairwise growth of inertial waves (Kerswell 1993). This offers an obvious candidate mechanism for the 'strong' instabilities which must exist to disrupt the solution and ultimately lead to the turbulent breakdown observed. Similarly strong flows are also seen experimentally in precessing cylinders (Gans 1970*a*; Manasseh 1992, 1994, 1996; Kobine 1995). One of the purposes of this paper is to investigate this 'strength' issue in the context of a simple planar model. Poincaré's solution possesses both elliptical and precessional strains, however, for Earthlike parameters, the precessional strain completely dominates the elliptical strain. Hence, it is entirely appropriate to focus upon the shearing of the fluid streamlines across each other, an effect which is readily captured in the plane layer model studied here. This, after all, is the generic precessional response of the fluid freed from boundary constraints (see Kerswell 1993 § 5).

There are many other questions surrounding the behaviour of strained rotating flows suggested by possible planetary applications. Geophysically, one of the most pertinent questions is whether precessing and tidal (elliptical) flows can exhibit sustained behaviour over 'slow' time scales. This is motivated by the desire to understand whether the temporal behaviour of the Earth's magnetic field, which is observed to vary over slow time scales of the order of the magnetic diffusion time for the Earth (15 000 years), could be influenced by such 'fast' (daily) processes. (As viewed from the rotating Earth, the tidal and precessional distortions have a daily frequency and, as will be seen, drive instabilities with frequencies of the same order.) The fact that e-folding times for growing inertial wave instabilities are typically on the magnetic diffusion time scale has already been pointed out (Kerswell 1994; Rieutord 2000; Seyed-Mahmoud, Henderson & Aldridge 2000). However, evidence that the nonlinear dynamics of these instabilities could also exhibit such long-term behaviour would be much more convincing of a possible connection.

There is also the question of whether tidally (elliptically) or precessionally driven electrically conducting fluid flows could act as 'dynamos', that is, could they generate and sustain a magnetic field against Ohmic dissipation. Although this particular issue is beyond the scope of the current paper, one of the underlying aims here will be to uncover parameter regimes where sufficiently complicated precessing flows exist to explore this possibility in later work. Experimental work by Gans (1970*b*) using liquid sodium has already indicated that precessing flows can significantly magnify ambient background fields. Other applications beyond our Earth potentially exist in the newly studied Galilean satellites (Kerswell & Malkus 1998; Showman & Malhotra 1999) and further afield still in newly discovered extra-solar planetary systems (Perryman 2000). The discovery of massive gaseous planets having very small orbital radii suggests that tides and precession may play a leading role in their dynamics and the generation of any magnetic field present.

One final reason for introducing and studying the precessing planar model here is its extendability to incorporate other physical effects. One particularly interesting issue is the effect of stable stratification on the precessional instability as a simple model of a precessing but non-convecting planetary core. Following the work of Gans (1970*b*),

the advection of an ambient magnetic field can also be studied as a possible model of Io's tidally-distorted fluid core which sits in Jupiter's magnetic field (Kerswell & Malkus 1998). Geophysically, the interaction of precessing and convecting flows is of particular interest since the Earth's core is convecting. Arguing on the basis of relevant time scales, there would appear to be little mechanistic overlap between the two. However, given the fact that precession is a persistent effect which can drive non-trivial, albeit rapidly fluctuating flows for long times, this seems dangerously simplistic.

The plan of the paper is as follows. Section 2 introduces the precessing plane layer model and discusses the strained rotating flow that is realized as the basic precessional response. The numerical formulation used to solve the equations is described in § 3. This is kept brief since the techniques used are largely standard. Section 4 discusses the asymptotic theory for the precessional instability in the limit of small precession rate. The instability occurs by two inertial waves resonating through the underlying strain field which is exactly the instability mechanism for elliptical flow. A linear time-stepping code is then used to extend this asymptotic theory to finite precession rates. The results of various nonlinear simulation runs showing how these instabilities evolve is then presented in § 5 followed by a final discussion in § 6.

2. Formulation

Consider the motion of a viscous fluid sandwiched between two plane boundaries at $Z = \pm\frac{1}{2}$ which are rotating (rapidly) with angular velocity $\hat{\boldsymbol{Z}}$ in a frame rotating (slowly) at angular velocity $\epsilon\hat{\boldsymbol{X}}$. In this precessing frame ($\boldsymbol{R} = X\hat{\boldsymbol{X}} + Y\hat{\boldsymbol{Y}} + Z\hat{\boldsymbol{Z}}$) the equations of motion (non-dimensionalized by the boundary spin rate ω and plate separation H) are

$$\frac{\partial \boldsymbol{U}}{\partial t} + 2\epsilon\hat{\boldsymbol{X}} \times \boldsymbol{U} + \boldsymbol{U} \cdot \nabla\boldsymbol{U} + \nabla P = E\nabla^2\boldsymbol{U}, \tag{2.1}$$

$$\nabla \cdot \boldsymbol{U} = 0, \tag{2.2}$$

with boundary conditions

$$\boldsymbol{U}(X, Y, \pm\tfrac{1}{2}) = \hat{\boldsymbol{Z}} \times \boldsymbol{R}, \tag{2.3}$$

where Ekman number $E = \nu/(\omega H^2)$ is the usual non-dimensionalization of the kinematic viscosity ν. For reasons which will quickly emerge, it is more convenient to work in the *boundary* (rotating, precessing) frame in which the boundaries are at rest (commonly called the 'mantle' frame in the context of the precessing Earth). Here, relative to the new axes ($x = X\cos t + Y\sin t, y = -X\sin t + Y\cos t, y, z = Z$), the equations of motion are

$$\frac{\partial \boldsymbol{u}}{\partial t} + 2[\hat{\boldsymbol{z}} + \boldsymbol{\epsilon}(t)] \times \boldsymbol{u} + \boldsymbol{u} \cdot \nabla\boldsymbol{u} + \nabla p = E\nabla^2\boldsymbol{u} + 2z\boldsymbol{\epsilon}(t), \tag{2.4}$$

$$\nabla \cdot \boldsymbol{u} = 0, \tag{2.5}$$

subject to the boundary conditions

$$\boldsymbol{u}(x, y, \pm\tfrac{1}{2}) = \boldsymbol{0}, \tag{2.6}$$

where

$$\boldsymbol{\epsilon}(t) = \epsilon\hat{\boldsymbol{X}} := \epsilon(\hat{\boldsymbol{x}}\cos t - \hat{\boldsymbol{y}}\sin t). \tag{2.7}$$

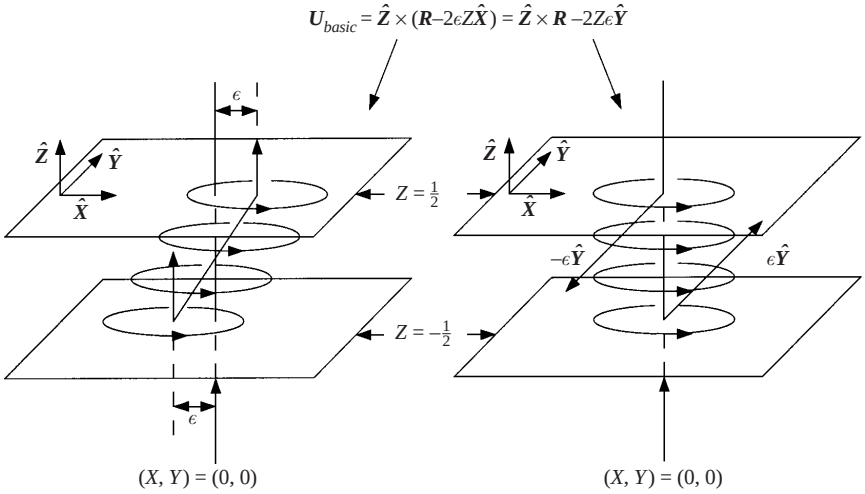

FIGURE 1. The basic state solution $\boldsymbol{U}_{basic}$ in the precessing frame. The velocity can either be viewed as circular streamlines parallel to the boundaries at $Z = \pm\frac{1}{2}$ but sheared in the $\hat{\boldsymbol{X}}$ direction (left-hand diagram), or as solid body rotation + a uniform shear in the $\hat{\boldsymbol{Y}}$ direction (right-hand diagram).

A simple flow solution exists to the equations of motion which has the form

$$\boldsymbol{U}_{basic} = \hat{\boldsymbol{Z}} \times (\boldsymbol{R} - 2\epsilon Z\,\hat{\boldsymbol{X}}) = -Y\,\hat{\boldsymbol{X}} + (X - 2\epsilon Z)\,\hat{\boldsymbol{Y}} \tag{2.8}$$

in the precessing frame and

$$\boldsymbol{u}_{basic} = 2[\boldsymbol{\epsilon}(t) \times \hat{\boldsymbol{z}}]\hat{\boldsymbol{z}} \cdot \boldsymbol{r} = -2\epsilon z(\hat{\boldsymbol{x}} \sin t + \hat{\boldsymbol{y}} \cos t) \tag{2.9}$$

in the boundary frame. This represents a uniformly strained rotating flow in which the streamlines remain circular (in the precessing frame), but where the vorticity is no longer perpendicular to the plane of motion (see figure 1). Another way to describe the flow is to note that the line connecting the centres of the circular streamlines is no longer perpendicular to the plane of the streamlines, or in other words, the circular streamlines are sheared across each other. This is the generic precessional response of a fluid and is realized in the interior of precessing containers where boundary layers typically fix up the boundary conditions (see Mahalov 1993 for the case of a precessing cylinder and Kerswell 1993 for a precessing spheroid). Here in this plane layer situation, weak $O(\epsilon)$ boundary layers are also required to compensate for the non-vanishing velocity of the basic flow at the boundaries. In what follows, we will ignore these layers in order to focus upon the stability of the sheared circular streamline structure set up in the interior. (Physically, it is possible to avoid such layers anyway by arranging for the two planar boundaries to have slightly different rotation centres, that is, the plate at $Z = \pm\frac{1}{2}$ is made to rotate at $\hat{\boldsymbol{Z}}$ about the point $\boldsymbol{R} = (\pm\epsilon, 0, \pm\frac{1}{2})$ rather than $\boldsymbol{R} = (0, 0, \pm\frac{1}{2})$.) Once this step is taken, the precessing fluid layer presents an excellent arena in which to study the flows that can be driven by interior strains since in the *boundary* frame the basic state is translationally invariant in both homogeneous directions. This is in contrast to the closely related case of elliptical flow in which the basic state would be

$$\boldsymbol{U}_{elliptical} = -(1 - \beta)Y\,\hat{\boldsymbol{X}} + (1 + \beta)X\,\hat{\boldsymbol{Y}}, \tag{2.10}$$

in the inertial frame where β measures the elliptical distortion and

$$\boldsymbol{u}_{elliptical} = \beta(x\sin 2t + y\cos 2t)\hat{\boldsymbol{x}} + \beta(x\cos 2t - y\sin 2t)\hat{\boldsymbol{y}}, \tag{2.11}$$

in the *boundary* or rotating frame. The elliptical perturbation is clearly not invariant under x or y translations and moreover becomes unbounded as either $|x|$ or $|y|$ becomes large. This makes studying elliptical flow in this context problematic. The difference between the two types of flow, however, is rather simple when viewed from cylindrical polar coordinates (s, ϕ, z); the basic state in elliptical flow corresponds to an $e^{2i\phi}$ perturbation of axisymmetric circular streamlines whereas the precessing basic state represents an $e^{i\phi}$ perturbation. As a result, the basic mechanism of linear instability is identical – parametric resonance of pairs of inertial waves – although the details vary – the exact pairs of waves which can resonate together are different. This means that we can expect much of the nonlinear dynamics revealed in precessing flows to carry over to elliptical flows.

In this paper, we solve for the deviation of the flow solution from the basic state. The governing equations for $\tilde{\boldsymbol{u}} := \boldsymbol{u} - \boldsymbol{u}_{basic}$ in the boundary frame are

$$\frac{\partial \tilde{\boldsymbol{u}}}{\partial t} + 2\hat{\boldsymbol{z}} \times \tilde{\boldsymbol{u}} + \tilde{\boldsymbol{u}} \cdot \nabla \tilde{\boldsymbol{u}} + \nabla \tilde{p} - E\nabla^2 \tilde{\boldsymbol{u}} = \epsilon \left\{ 2z\left[\sin t \frac{\partial}{\partial x} + \cos t \frac{\partial}{\partial y}\right] + \begin{bmatrix} 0 & 0 & 4\sin t \\ 0 & 0 & 4\cos t \\ -2\sin t & -2\cos t & 0 \end{bmatrix} \right\} \tilde{\boldsymbol{u}}, \tag{2.12}$$

$$\nabla \cdot \tilde{\boldsymbol{u}} = 0, \tag{2.13}$$

which we solve subject to the stress-free boundary conditions

$$\frac{\partial \tilde{u}}{\partial z} = \frac{\partial \tilde{v}}{\partial z} = \tilde{w} = 0 \quad \text{on} \quad z = \pm\tfrac{1}{2}. \tag{2.14}$$

These rather than the more natural non-slip conditions are used to avoid Ekman boundary layers which would be numerically expensive to resolve. Additionally, the inertial waves used to discuss the instability mechanism in § 4 automatically satisfy stress-free boundary conditions. This helps focus attention on the instability mechanism in the interior rather than on what are secondary details at the boundaries.

3. Numerics

Solutions to the system (2.12)–(2.14) are sought which are periodic in both the x-direction (period $2\pi/k_x$) and the y-direction (period $2\pi/k_y$). The fundamental wavenumbers k_x and k_y are chosen to facilitate the precessional response of the fluid in a way to be discussed below. The velocity field is decomposed into toroidal and poloidal parts together with mean horizontal components,

$$\tilde{\boldsymbol{u}} = \nabla \times e(\boldsymbol{x}, t)\hat{\boldsymbol{z}} + \nabla \times \nabla \times f(\boldsymbol{x}, t)\hat{\boldsymbol{z}} + U_x(z, t)\hat{\boldsymbol{x}} + U_y(z, t)\hat{\boldsymbol{y}}, \tag{3.1}$$

so that incompressibility is enforced *ab initio*. The scalar equations for e, f, U_x and U_y are $\hat{\boldsymbol{z}} \cdot \nabla \times$ (2.12), $\hat{\boldsymbol{z}} \cdot \nabla \times \nabla \times$ (2.12), $\hat{\boldsymbol{x}} \cdot$ (2.12) and $\hat{\boldsymbol{y}} \cdot$ (2.12) where

$$\overline{A} := \frac{k_x k_y}{4\pi^2} \int_0^{2\pi/k_x} \int_0^{2\pi/k_y} A \, \mathrm{d}y \, \mathrm{d}x \tag{3.2}$$

is the horizontal average, which are to be solved subject to the boundary conditions

$$f = \frac{\partial^2 f}{\partial z^2} = \frac{\partial e}{\partial z} = \frac{\partial U_x}{\partial z} = \frac{\partial U_y}{\partial z} = 0. \tag{3.3}$$

The method of solution is one of Galerkin-projection in x and y and collocation over z using the spectral expansions

$$e := \sum_{l=-N_x+1}^{N_x} \sum_{m=-N_y+1}^{N_y} \sum_{n=1}^{N_z} e_{lmn}(t) \exp \mathrm{i}(lk_x x + mk_y y)\phi_n(2z), \tag{3.4}$$

$$f := \sum_{l=-N_x+1}^{N_x} \sum_{m=-N_y+1}^{N_y} \sum_{n=1}^{N_z} f_{lmn}(t) \exp \mathrm{i}(lk_x + mk_y y)\psi_n(2z), \tag{3.5}$$

$$U_x := \sum_{n=1}^{N_z} U_{xn}(t)\phi_n(2z), \quad U_y := \sum_{n=1}^{N_z} U_{yn}(t)\phi_n(2z). \tag{3.6}$$

The expansion functions in z are defined as follows

$$\phi_n(z) := T_{n-1}(z) - \frac{(n-1)^2}{(n+1)^2} T_{n+1}(z),$$

$$\psi_n(z) := T_{n-1}(z) - \frac{2(n+1)(2n^2+4n+9)}{(n+2)(2n^2+8n+9)} T_{n+1}(z) + \frac{n(2n^2+1)}{(n+2)(2n^2+8n+9)} T_{n+3}(z)$$

with

$$T_n(z) := \cos(n \cos^{-1} z) \tag{3.7}$$

being the Chebyshev polynomial of degree n, so that they individually satisfy the appropriate boundary conditions. For given truncation (N_x, N_y, N_z) there are $2N_z(1 + 2N_y + 4N_yN_x)$ degrees of freedom since U_{xn} and U_{yn} are real coefficients and the complex coefficients e and f satisfy $e_{00n} = f_{00n} = 0$, $e_{-l-mn} = e^*_{lmn}$ and $f_{-l-mn} = f^*_{lmn}$ where * indicates complex conjugation. A typical truncation level used in this paper was $(N_x, N_y, N_z) = (8, 8, 32)$ corresponding to 17 472 degrees of freedom and the largest used was $(N_x, N_y, N_z) = (16, 16, 32)$ with 67 648 degrees of freedom. No particular symmetries were imposed upon the solutions so that perfectly general velocity fields could develop, albeit within the chosen periodic box $0 \leqslant x \leqslant 2\pi/k_x$, $0 \leqslant y \leqslant 2\pi/k_y$. The fact that the basic solution has a definite parity about the midplane in z, however, was exploited by splitting each of the dependent variable expansions into even and odd parts and dealing with each separately. Although this doubled the number of discretization matrices, it also halved their size hence doubling the speed of the code.

The spectral equations were integrated forward in time using a second-order Adams–Bashforth scheme for the advective and precessional terms and a second-order Crank–Nicolson scheme for the diffusive terms. The nonlinear terms were calculated in physical space with optimized fast Fourier transform routines being used to transfer between spectral and physical space. These are standard practices for numerical solution of such systems (see, for example, Jones & Roberts 2000). A typical runtime for the code at truncation level $(N_x, N_y, N_z) = (8, 8, 32)$ to cover 10 fast rotation periods was 11.3 min on an Alpha 21264A 667 MHz processor taking a time step $\Delta t = 2\pi/1000$ and using a memory of 10 MB. For $(N_x, N_y, N_z) = (16, 16, 32)$, the largest run ever undertaken, these numbers jump to 87.3 min and 24 MB. The

time step has to be chosen so small to resolve the inertial oscillations inherent in the system – this is a classically stiff problem.

Various physical quantities were output as the code ran. Defining the bulk average as

$$\langle A\rangle := \int_{-1/2}^{1/2} \mathrm{d}z\, \overline{A} = \frac{k_x k_y}{4\pi^2} \int_0^{2\pi/k_x} \mathrm{d}x \int_0^{2\pi/k_y} \mathrm{d}y \int_{-1/2}^{1/2} \mathrm{d}z A, \tag{3.8}$$

the long-time averages of the global kinetic energy of the velocity disturbance

$$K := \frac{1}{T-T_0} \int_{T_0}^{T} K(t) := \langle \tfrac{1}{2}\tilde{\boldsymbol{u}}^2\rangle \,\mathrm{d}t \tag{3.9}$$

and the total power dissipation

$$D := \frac{1}{T-T_0} \int_{T_0}^{T} D(t) := 2E\langle e_{ij}e_{ij}\rangle \,\mathrm{d}t, \tag{3.10}$$

were used as global measures of the velocity solution where T_0 is appropriately chosen to be beyond initial transients and $e_{ij} := \frac{1}{2}(u_{i,j} + u_{j,i})$ is the rate of strain tensor. The ratio of the root-mean-square of the disturbance velocity to the basic velocity,

$$I := \frac{\sqrt{\langle \tilde{\boldsymbol{u}}^2\rangle}}{\sqrt{\langle \boldsymbol{u}_{basic}^2\rangle}} = \frac{\sqrt{6K}}{\epsilon}, \tag{3.11}$$

was used to measure the strength of the instability, whereas $D/D_{basic} = D/(4E\epsilon^2)$ gave a measure of the dissipative efficiency. To help diagnose the character of the solutions, the energies $E_{lm}(t)$ associated with each Fourier mode (l,m) and the mean flow components $E_{00} = \langle \frac{1}{2}(U_x^2 + U_y^2)\rangle$ were also output as was the value of $Re(\tilde{w})$ at the arbitrary point $(x,y,z) = (0,0,1/2\sqrt{2})$ for the purposes of generating a (typical) time series of the flow evolution.

4. Linear results

4.1. *Linear instability: theory*

The precessional instability mechanism is inertial in character and hence is most clearly understood by ignoring viscosity in the problem (2.12)–(2.14). Linearizing to consider small disturbances further simplifies the system to

$$\frac{\partial \tilde{\boldsymbol{u}}}{\partial t} + 2\hat{\boldsymbol{z}} \times \tilde{\boldsymbol{u}} + \nabla \tilde{p} = \epsilon[\mathrm{e}^{\mathrm{i}t}\mathscr{L} + \mathrm{e}^{-\mathrm{i}t}\mathscr{L}^*]\tilde{\boldsymbol{u}}, \tag{4.1}$$

where

$$\mathscr{L} := \begin{bmatrix} z(\partial_y - \mathrm{i}\partial_x) & 0 & -2\mathrm{i} \\ 0 & z(\partial_y - \mathrm{i}\partial_x) & 2 \\ \mathrm{i} & -1 & z(\partial_y - \mathrm{i}\partial_x) \end{bmatrix}, \tag{4.2}$$

with

$$\nabla \cdot \tilde{\boldsymbol{u}} = 0, \quad \tilde{w}(x,y,\pm\tfrac{1}{2}) = 0. \tag{4.3}$$

When $\epsilon = 0$, equation (4.1) reduces to the inertial wave problem (Greenspan 1968) for which a complete set of normal modes or inertial waves exist of the form

$$\begin{bmatrix} u \\ v \\ w \\ p \end{bmatrix} = \begin{pmatrix} k^2(k_x\lambda - 2\mathrm{i}k_y)\cos(n\pi[z+\frac{1}{2}])/4k_\perp^2 \\ k^2(k_y\lambda + 2\mathrm{i}k_x)\cos(n\pi[z+\frac{1}{2}])/4k_\perp^2 \\ -\mathrm{i}k_z\sin(n\pi[z+\frac{1}{2}])/\lambda \\ \cos(n\pi[z+\frac{1}{2}]) \end{pmatrix} \exp(\mathrm{i}(k_x x + k_y y + \lambda t)) \tag{4.4}$$

with $k_\perp^2 := k_x^2 + k_y^2$, $k_z := n\pi$, $k^2 := k_\perp^2 + k_z^2$ and the dispersion relation is

$$\lambda = \frac{\pm 2k_z}{k}, \tag{4.5}$$

where $n = 0, 1, 2, \ldots$ and $k_x, k_y \in \mathbb{R}$. For $0 < \epsilon \ll 1$, the right-hand side of (4.1) acts as a small coupling term between these neutral inertial modes which can lead to secular growth on the $O(1/\epsilon)$ time scale. To see this, introduce a slow timescale $\tau = \epsilon t$ and consider a linear combination of two inertial waves ($\lambda_A \neq \lambda_B$),

$$\tilde{\boldsymbol{u}} = A(\tau)\boldsymbol{u}_A(\boldsymbol{x})\exp(\mathrm{i}\lambda_A t) + B(\tau)\boldsymbol{u}_B(\boldsymbol{x})\exp(\mathrm{i}\lambda_B t) + \epsilon\tilde{\boldsymbol{v}}(\boldsymbol{x}, t) + \cdots \tag{4.6}$$

to leading order in ϵ. The lowest $O(1)$ version of (4.1) confirms that the amplitudes A and B are independent of the fast time t. At next order, $O(\epsilon)$,

$$\begin{aligned} \frac{\partial\tilde{\boldsymbol{v}}}{\partial t} + 2\hat{\boldsymbol{z}}\times\tilde{\boldsymbol{v}} + \nabla\tilde{p} = {} & A[\exp(\mathrm{i}(\lambda_A+1)t)\mathscr{L} + \exp(\mathrm{i}(\lambda_A-1)t)\mathscr{L}^*]\boldsymbol{u}_A(\boldsymbol{x}) \\ & + B[\exp(\mathrm{i}(\lambda_B+1)t)\mathscr{L} + \exp(\mathrm{i}(\lambda_B-1)t)\mathscr{L}^*]\boldsymbol{u}_B(\boldsymbol{x}) \\ & - A_\tau\boldsymbol{u}_A\exp(\mathrm{i}\lambda_A t) - B_\tau\boldsymbol{u}_B\exp(\mathrm{i}\lambda_B t). \end{aligned} \tag{4.7}$$

The slow variation of the amplitudes A and B is determined by the elimination of any secularity in $\tilde{\boldsymbol{v}}$. Introducing the inner product

$$\langle\boldsymbol{u}, \boldsymbol{v}\rangle := \lim_{L\to\infty}\frac{1}{4L^2}\int_{-L}^{L}\int_{-L}^{L}\int_{-1/2}^{1/2}\boldsymbol{u}^*\cdot\boldsymbol{v}\,\mathrm{d}z\,\mathrm{d}y\,\mathrm{d}x, \tag{4.8}$$

under which inertial waves are orthogonal, then $\langle\boldsymbol{u}_A\exp(\mathrm{i}\lambda_A t), (4.7)\rangle$ requires that

$$A_\tau\langle\boldsymbol{u}_A, \boldsymbol{u}_A\rangle = B\langle\boldsymbol{u}_A, [\exp(\mathrm{i}(\lambda_B - \lambda_A + 1)t)\mathscr{L} + \exp(\mathrm{i}(\lambda_B - \lambda_A - 1)t)\mathscr{L}^*]\boldsymbol{u}_B\rangle, \tag{4.9}$$

all other terms necessarily being non-secular. Clearly, the case of interest is when $\lambda_B = \lambda_A \pm 1$ and without loss of generality, we choose $\lambda_B = \lambda_A + 1$, so that (4.9) and $\langle\boldsymbol{u}_B\exp(\mathrm{i}\lambda_B t), (4.7)\rangle$ then give

$$A_\tau\langle\boldsymbol{u}_A, \boldsymbol{u}_A\rangle = B\langle\boldsymbol{u}_A, \mathscr{L}^*\boldsymbol{u}_B\rangle, \quad B_\tau\langle\boldsymbol{u}_B, \boldsymbol{u}_B\rangle = A\langle\boldsymbol{u}_B, \mathscr{L}\boldsymbol{u}_A\rangle. \tag{4.10}$$

These amplitude equations have secularly growing solutions $(A, B) = (A_0, B_0)\mathrm{e}^{\sigma\epsilon t}$ provided

$$\sigma^2 = \frac{\langle\boldsymbol{u}_A, \mathscr{L}^*\boldsymbol{u}_B\rangle\langle\boldsymbol{u}_B, \mathscr{L}\boldsymbol{u}_A\rangle}{\langle\boldsymbol{u}_A, \boldsymbol{u}_A\rangle\langle\boldsymbol{u}_B, \boldsymbol{u}_B\rangle} \tag{4.11}$$

is positive. The numerator vanishes unless the inertial waves $\boldsymbol{u}_A$ and $\boldsymbol{u}_B$ have (i) exactly the same wavenumbers (k_x, k_y) and (ii) opposite parity in z, i.e. $n_B - n_A = 1 \bmod 2$.

$n_A \rightarrow$ $n_B \downarrow$	1	2	3	4	5	6	7	8
1	$\ddots$	18.059	—	29.352	—	40.433	—	51.434
2	0.3547	$\ddots$	30.304	—	41.838	—	53.117	—
3	—	0.3743	$\ddots$	42.504	—	54.176	—	65.596
4	0.0948	—	0.3797	$\ddots$	54.690	—	66.456	—
5	—	0.1115	—	0.3819	$\ddots$	66.868	—	78.691
6	0.0479	—	0.1182	—	0.3830	$\ddots$	79.044	—
7	—	0.0598	—	0.1216	—	0.3836	$\ddots$	91.217
8	0.0300	—	0.0656	—	0.1236	—	0.3840	$\ddots$

TABLE 1. Asymptotic growth rates σ (below the leading diagonal) and unstable wavenumbers $k_\perp$ (above the leading diagonal) for precessional instabilities of type 1. These results are plotted in a single table since they are identical if the values of n_A and n_B are interchanged.

Assuming these 'resonant' conditions hold, the inner products in (4.11) evaluate to

$$\langle \boldsymbol{u}_A, \mathscr{L}^* \boldsymbol{u}_B \rangle = (k_x - \mathrm{i}k_y) \left\{ \mathscr{Q} - \frac{n_B^2 k_A^2 (2 - \lambda_A)}{2(n_B^2 - n_A^2)\lambda_B k_\perp^2} \right\}, \tag{4.12}$$

$$\langle \boldsymbol{u}_B, \mathscr{L} \boldsymbol{u}_A \rangle = (k_x + \mathrm{i}k_y) \left\{ -\mathscr{Q} + \frac{n_A^2 k_B^2 (2 + \lambda_B)}{2(n_B^2 - n_A^2)\lambda_A k_\perp^2} \right\}, \tag{4.13}$$

where

$$\mathscr{Q} = \frac{(n_A^2 + n_B^2) k_A^2 k_B^2 (4 + \lambda_A \lambda_B)}{8(n_B^2 - n_A^2)^2 \pi^2 k_\perp^2} - \frac{n_A^2 k_B^2 (2 + \lambda_B)\lambda_B + n_B^2 k_A^2 (2 - \lambda_A)\lambda_A}{2(n_B^2 - n_A^2) k_\perp^2 \lambda_A \lambda_B} + \frac{4 n_A^2 n_B^2}{(n_B^2 - n_A^2)^2 \lambda_A \lambda_B}, \tag{4.14}$$

and

$$\langle \boldsymbol{u}_A, \boldsymbol{u}_A \rangle = \frac{k_A^4}{4k_\perp^2}, \quad \langle \boldsymbol{u}_B, \boldsymbol{u}_B \rangle = \frac{k_B^4}{4k_\perp^2}. \tag{4.15}$$

The numerator in (4.11) also vanishes if either n_A or n_B is zero. This means that the exceptional inertial wave with $n = \lambda = 0$ present here in this planar geometry never participates in a precessional instability. For other pairs of inertial waves, three types of precessional instability can be identified as follows:

1. $-1 < \lambda_A < 0 < \lambda_B < 1$ unique $k_\perp^2$ any $n_A \neq n_B \neq 0$
2. $0 < \lambda_A < 1 < \lambda_B < 2$ two solutions $k_\perp^2 < k_0^2$, $k_\perp^2 > k_0^2$ if $n_B > n_A(2 + \sqrt{5})$
3. $-2 < \lambda_A < -1 < \lambda_B < 0$ two solutions $k_\perp^2 < k_0^2$, $k_\perp^2 > k_0^2$ if $n_A > n_B(2 + \sqrt{5})$

where $k_0^2 := \pi^2 n_B^{2/3} n_A^{2/3} (n_B^{2/3} + n_A^{2/3})$.

The most important precessional resonances are of type 1 with $-1 < \lambda_A < 0 < \lambda_B < 1$. In fact, for all instabilities of types 2 and 3 we considered we found $\sigma^2 < 0$, so that precession simply shifts the frequency of the underlying inertial waves rather than leading to unstable growth. Table 1 shows the unstable wavenumbers $k_\perp$ and

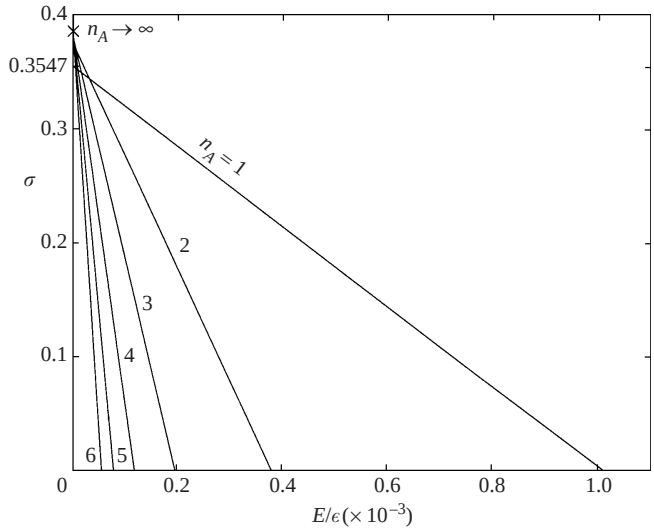

FIGURE 2. Asymptotic $(E, \epsilon \to 0)$ growth rates σ as a function of E/ϵ for precessional resonances with $n_B = n_A + 1$. $\times$, asymptotic supremum growth rate $5\sqrt{15}/16\pi^{-1}$, and 0.3547 is the maximum growth rate for $n_A = 1$.

growth rates σ for some possible resonances of type 1, where $k_\perp$ is the unique solution of $\lambda_A + 1 = \lambda_B$ for given n_A and n_B, and σ is given by (4.11). From table 1 we see that the largest growth rates manifest themselves for $n_B = n_A + 1$ when the inertial waves 'overlap' most strongly. The growth rates for these resonances increase monotonically as $n_A \to \infty$, ultimately approaching the asymptotic growth rate supremum of $5\sqrt{15}/16\,\pi^{-1} \approx 0.385$. This is a factor of $2/\pi$ smaller than the maximum growth rate of $5\sqrt{15}/32 \approx 0.605$ possible in an unbounded precessing fluid (Kerswell 1993) and is an indication that the slight mismatch in z-structure between the resonating waves is always significant.

The presence of viscosity acts to suppress small scales which here translates into precessional instabilities with large n_A and n_B (note from table 1 that larger n_A and n_B also have larger values of $k_\perp$). The viscous damping rate of an inertial wave is just Ek^2 for stress-free boundary conditions so that the leading-order viscous correction to the amplitude equations, (4.10), is:

$$\left(A_\tau + \frac{E}{\epsilon}k_A^2 A\right)\langle \boldsymbol{u}_A, \boldsymbol{u}_A\rangle = B\langle \boldsymbol{u}_A, \mathscr{L}^*\boldsymbol{u}_B\rangle, \qquad \left(B_\tau + \frac{E}{\epsilon}k_B^2 B\right)\langle \boldsymbol{u}_B, \boldsymbol{u}_B\rangle = A\langle \boldsymbol{u}_B, \mathscr{L}\boldsymbol{u}_A\rangle. \tag{4.16}$$

For more physical non-slip boundary conditions, the viscous damping rate is $O(E^{1/2})$. For each case considered in § 5, we actually have $Ek^2 = O(E^{1/2})$, so the two damping rates are comparable. Instability can now only arise if the inviscid growth rate $\sigma\epsilon$ given by (4.11) exceeds the geometric mean of the viscous decay rates,

$$\sigma\epsilon > Ek_A k_B. \tag{4.17}$$

The precessional instabilities with large n_A and n_B are therefore preferentially damped so that the type 1 instability with $n_A = 1, n_B = 2$ has effectively the largest growth rate for the largest range of parameters as illustrated in figure 2. Here, attention will be focused exclusively on this particular precessional instability where $k_\perp = 18.059$ with $n_A = 1$, $\lambda_A = -0.3428$, $n_B = 2$, $\lambda_B = 0.6572$ and $\sigma = 0.3547$ in the limit $\epsilon \to 0$. This

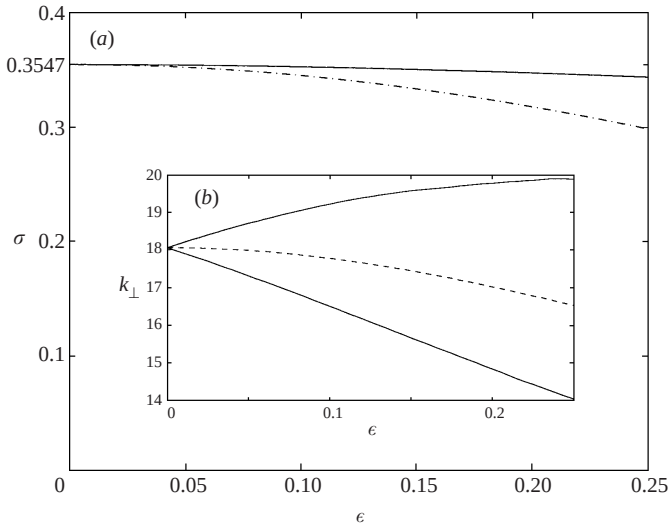

FIGURE 3. Numerically determined growth rates σ for finite ϵ ($E = 0$) for the $n_A = 1$, $n_B = 2$ instability. (*a*) Values of —, σ_{max} and — · —, $\sigma(k_\perp = 18.059)$ where 18. 059 is the asymptotic ($\epsilon \to 0$) optimal value of $k_\perp$. (*b*) The instability tongue emanating from this point in wavenumber space (– – –, $k_\perp$ which gives the maximum growth rate).

enables us to concentrate on the simplest precessional flow where only two inertial waves are excited by the initial linear instability. Consideration of table 1 shows that much more complicated scenarios may arise for alternative choices of $k_\perp$. 'De-tuning' at finite parameters often enables unstable growth over a range of wavenumbers surrounding the asymptotic value (see, for example, figure 3(*b*) where unstable growth can exist for $k_\perp \in (14.04, 19.89)$ at $\epsilon = 0.25$). It is therefore quite possible that $k_\perp \approx 30$ may excite resonances $n_A = 2, n_B = 3$, and $n_A = 1, n_B = 4$ simultaneously, whereas $k_\perp \approx 41$ could excite any or all of $n_A = 3, n_B = 4$, $n_A = 2, n_B = 5$ and $n_A = 1, n_B = 6$, provided the Ekman number is sufficiently small. Consideration of such systems is left for future investigation.

4.2. *Linear instability: numerics*

To check and extend the asymptotic theory described above, the linear timestepping code was adapted to apply Floquet stability analysis to the time-periodic basic flow (2.9) at *finite* ϵ ($E = 0$). This produced excellent agreement in the limit $\epsilon \to 0$ with the theoretical growth rates deduced above. Figure 3 shows the instability tongue which emanates from the asymptotic resonance point $k_\perp = 18.059$, $\sigma = 0.3547$ for the instability ($n_A = 1, n_B = 2$) of interest. The Floquet code also proved an ideal way to generate initial conditions at finite precession ϵ and Ekman number E for the nonlinear time-stepping calculations described below. For simplicity, the periodicity of the numerical domain was always chosen to reflect the asymptotically optimal horizontal wavelength $k_\perp = 18.059$ for the fastest growing mode ($n_A = 1, n_B = 2$). Although this was no longer the strictly optimal $k_\perp$ at the finite ϵ and E used, its corresponding growth rate was always close to maximal over the precession rates used, as is evident in figure 3(*a*). A final use of the Floquet code was to examine the structure of the linearly unstable flow. Visualizations of the velocity field in the (y, z)-plane showed a very clear 'two-cell' structure in each velocity component. Although

these were insensitive to amplitude, they provided a useful reference for subsequent visualizations of the nonlinear flow.

5. Nonlinear results

Following the validation of the linear time-stepping code using the asymptotic theory, the nonlinear code was checked for energetic consistency. A comparison was made between the disturbance kinetic energy at a given time calculated from the time-stepped velocity (i.e. the PDE) with that determined by directly time-integrating the kinetic energy evolution equation ($\langle \tilde{\boldsymbol{u}} \cdot (2.12) \rangle$ an ODE). The error was typically less than 1 part in 1000 over 30 fast rotation periods or revolutions using a time step $\Delta t = 2\pi/1000$. Over longer time intervals, the level of agreement between the two energies depended on the behaviour of the developing flow. Flows with small energetic variation of say $\pm 50\%$ about a mean level continued to have excellent agreement, with errors often less than 1 part in 10 over $O(1000)$ rotation periods. Flows with energies varying over several orders of magnitude, however, had larger relative errors. This is not surprising as errors are accumulated as the ODE is integrated in time, and an error that would be considered small at a local maximum, can easily dominate the ODE solution at local minima. Nonetheless, the qualitative behaviour of the PDE and ODE energies gave good evidence that solutions were energetically consistent.

5.1. *Two-dimensional nonlinear results*

The time-stepping code was initially optimized to allow only two-dimensional flow fields in order to gain some first insight into the nonlinear evolution of the precessional instability. Specifically, the spectral expansions for the toroidal and poloidal parts were restricted to

$$e := \sum_{m=-N_y+1}^{N_y} \sum_{n=1}^{N_z} e_{mn}(t) \exp \mathrm{i}(mk_y y)\, \phi_n(2z), \quad f := \sum_{m=-N_y+1}^{N_y} \sum_{n=1}^{N_z} f_{mn}(t) \exp \mathrm{i}(mk_y y) \psi_n(2z),$$

so that for a given truncation (N_y, N_z), there were now only $2N_z(1 + 2N_y)$ degrees of freedom. The numerical domain was defined by setting the primary wavenumber $k_y = k_\perp$ for the fastest growing $(n_A = 1, n_B = 2)$ linear instability and the corresponding eigenfunction was used as the initial condition. Two parameter regimes were studied: a weakly precessing situation $E = 10^{-5}$, $\epsilon \in [0.009885, 0.028]$ and a strongly precessing situation $E = 5 \times 10^{-5}$, $\epsilon \in [0.04996, 0.24]$. Owing to the reduced stiffness of the latter system, only this proved practical to continue studying using the fully three-dimensional code.

Weakly precessing case: $E = 10^{-5}$, $\epsilon \in [0.009885, 0.028]$

This parameter regime was studied to clarify the weakly nonlinear behaviour of the instability. Weakly nonlinear simulations carried out for an elliptically distorted rotating cylinder (Mason & Kerswell 1999) already indicate that a growing elliptical instability undergoes a secondary supercritical Hopf bifurcation once it reaches sufficient amplitude. Similar behaviour should be expected for the precessional instability considered here.

Figures 4 and 5 show how the energies and dissipations of the end-state solutions found vary over the studied range. There are four separate solution branches and

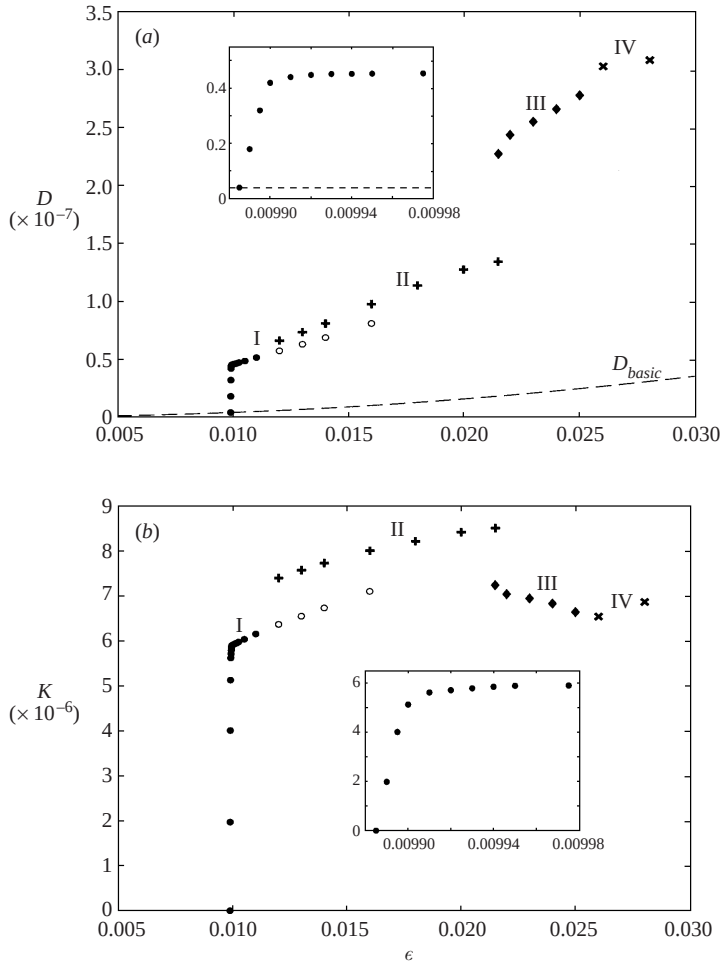

FIGURE 4. Weakly precessing case: $E = 10^{-5}$. (a) Total dissipation D ($D_{basic} = 4E\epsilon^2$ is shown as the dotted line), and (b) perturbation kinetic energy K for the solution branches, ●, I; +, II; ◆, III; ×, IV. In this and all subsequent similar plots solid markers (or in the case of + and ×, thicker markers) represent stable solutions and hollow markers (thin in the case of + and ×) represent unstable solutions. Each subplot shows a zoom of the initial bifurcation at $\epsilon \gtrsim \epsilon_{crit}$.

the flow shows two well-defined trends. The total dissipation D increases with precession rate (figure 4a) whereas the strength I of the instability decreases (figure 5b). Effectively, the flow becomes more efficient in dissipating energy. The 'lowest' or first branch (I) touches the ϵ-axis at $\epsilon_{crit} = 0.009885$ and represents the saturated nonlinear state of the two unstable inertial waves. This is clear from the power spectrum in figure 6(a), where the inertial frequencies at $-\lambda_A = 0.3428$ and $\lambda_B = 0.6572$ are clearly visible.

Perhaps the most striking feature of figures 4 and 5 (and the subplots therein) is the very narrow ϵ-interval over which the bifurcating flow from ϵ_{crit} (branch I) climbs to a finite amplitude. Coincidentally, this steep ascent has been seen before in the different context of a doubly rotating infinite pipe of fluid (figure 14 of Barnes & Kerswell 2000). Since weakly nonlinear theory essentially holds for as long as the kinetic energy K increases linearly off the axis (since $|\tilde{\boldsymbol{u}}| \sim (\epsilon - \epsilon_{crit})^{1/2}$ implies $K \sim \epsilon - \epsilon_{crit}$) we can

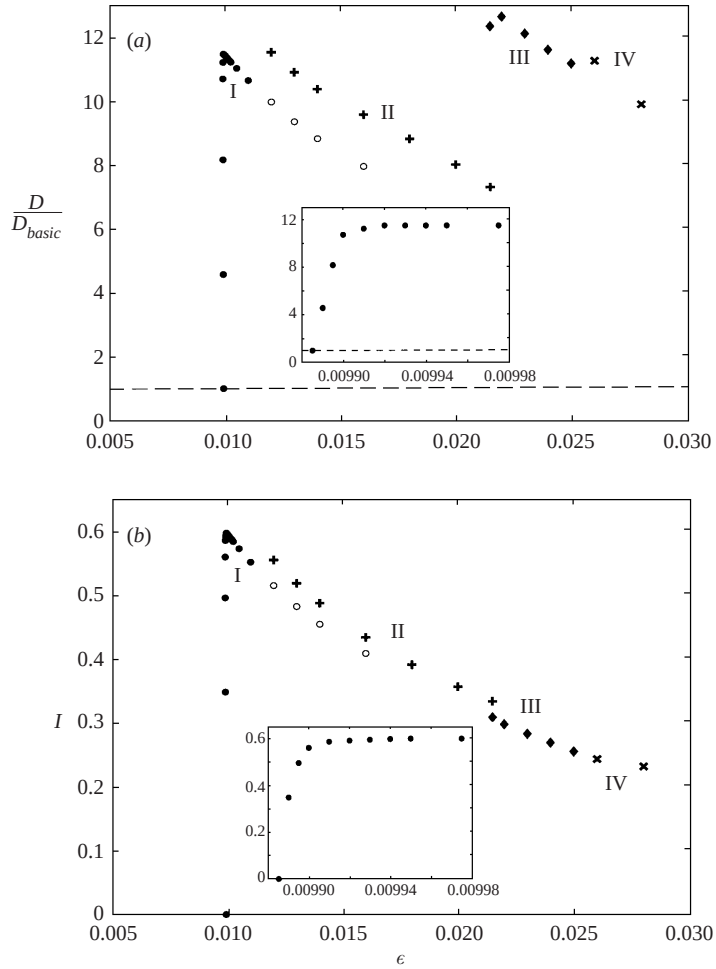

FIGURE 5. Weakly precessing case: $E = 10^{-5}$. (*a*) Ratio of dissipation D to D_{basic} and (*b*) intensity I, for the four solution branches I to IV.

estimate the interval over which this theory is valid. From the subplots of figures 4(*b*) and 5(*b*), the linear increase of K appears to stop when $I = O(1)$ or $|\tilde{\boldsymbol{u}}| = O(\epsilon)$ so that

$$(\epsilon - \epsilon_{crit})^{1/2} = \beta\epsilon, \tag{5.1}$$

where β is an $O(1)$ parameter. This means that we can estimate that weakly nonlinear theory holds only over an interval of $O(\epsilon_{crit}^2)$. Furthermore, from figures 4 and 5, since the end of this region is $\epsilon \approx 0.0099$, β can be estimated as ≈ 0.39. To add weight to this estimation procedure, we find below that a similar argument applied in a situation where ϵ_{crit} is five times larger gives rise to a very similar value of β ($\beta \approx 0.34$).

After branch I has climbed to a level where $I = O(1)$, it loses stability through a supercritical Hopf bifurcation at least by $\epsilon = 0.012$ where the second branch (II) is shown to start. In fact, examining the power spectrum of the time series for $\epsilon = 0.0105$ shown in figure 6(*a*) indicates that branch I is already unstable there, although the saturated secondary amplitude is too small to be seen in a time history of the evolution. This secondary amplitude is certainly visible at $\epsilon = 0.016$ as shown in

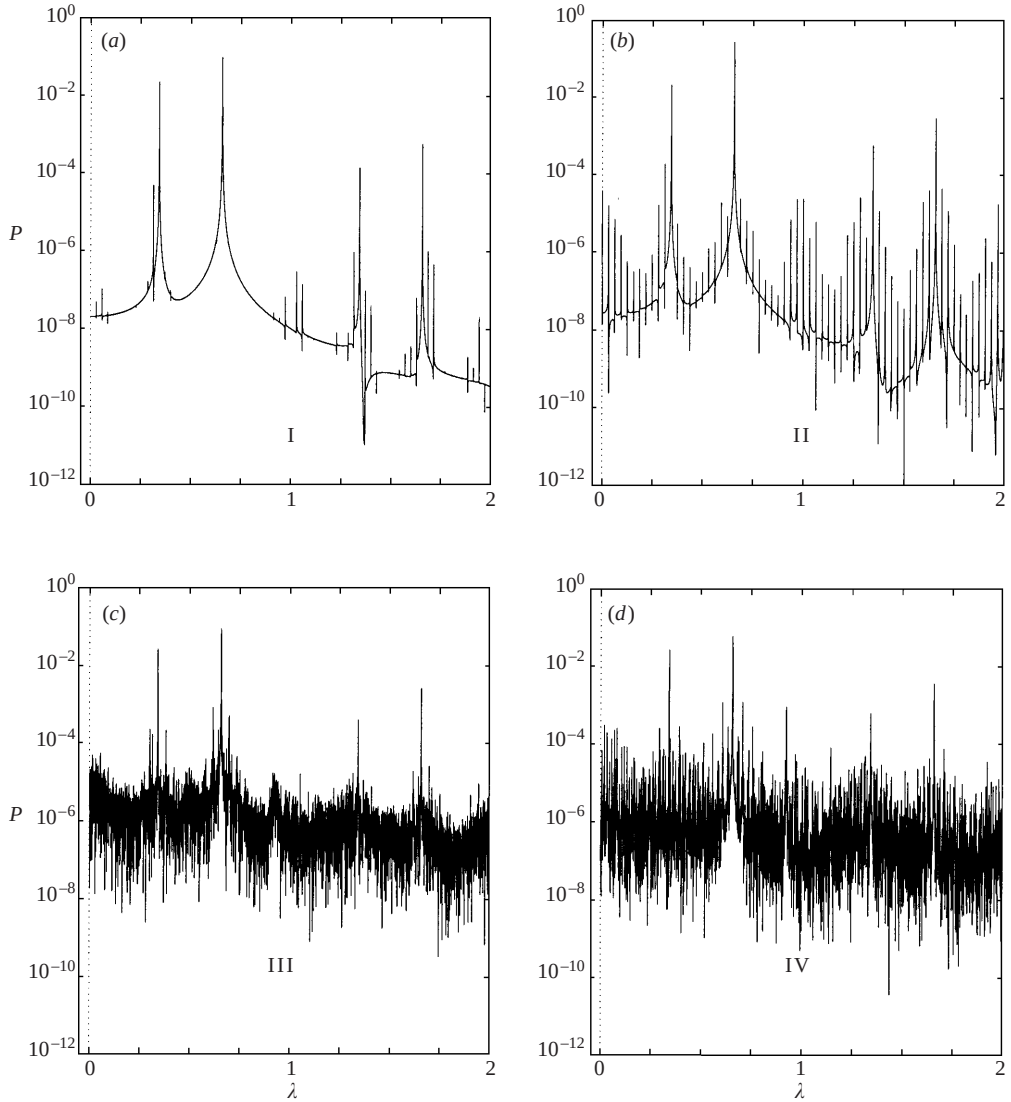

FIGURE 6. Weakly precessing case: $E = 10^{-5}$. In this and all similar subsequent plots (excluding Figure 8) the power spectra P of the solution branches was calculated by taking a Fourier transform of a ($\sim 1000 \rightarrow 5000$ rev) time series for the typical velocity $w(0, 0, 1/2\sqrt{2})$. $\lambda = 1$ is the frequency of the basic state solution (2.9). (*a*) Branch I solution for $\epsilon = 0.0105$ taken for $t > 3000$ rev. (*b*) Branch II solution for $\epsilon = 0.016$ taken for $t > 4000$ rev. (*c*) Branch III solution for $\epsilon = 0.024$ taken for $t > 1000$ rev. (*d*) Branch IV solution for $\epsilon = 0.028$ taken for $t > 500$ rev.

figure 7(*a*) where a transition from branch I to II is clear for $N > 3000$ (a typical time series of Fourier energy levels in figure 7(*b*) shows that the run is adequately resolved by $(N_y, N_z) = (16, 32)$). Figure 6(*b*), which is the corresponding power spectrum calculated for $t > 4000$ rev, clearly shows the emergence of this new periodicity in the flow as although the inertial frequencies are still clear, so is a new slow frequency. Beyond $\epsilon = 0.016$, the secondary instability appears so quickly that the level of the primary branch can no longer be distinguished.

Branch II persists until $\epsilon = 0.0215$ when a new third branch (III) of enhanced

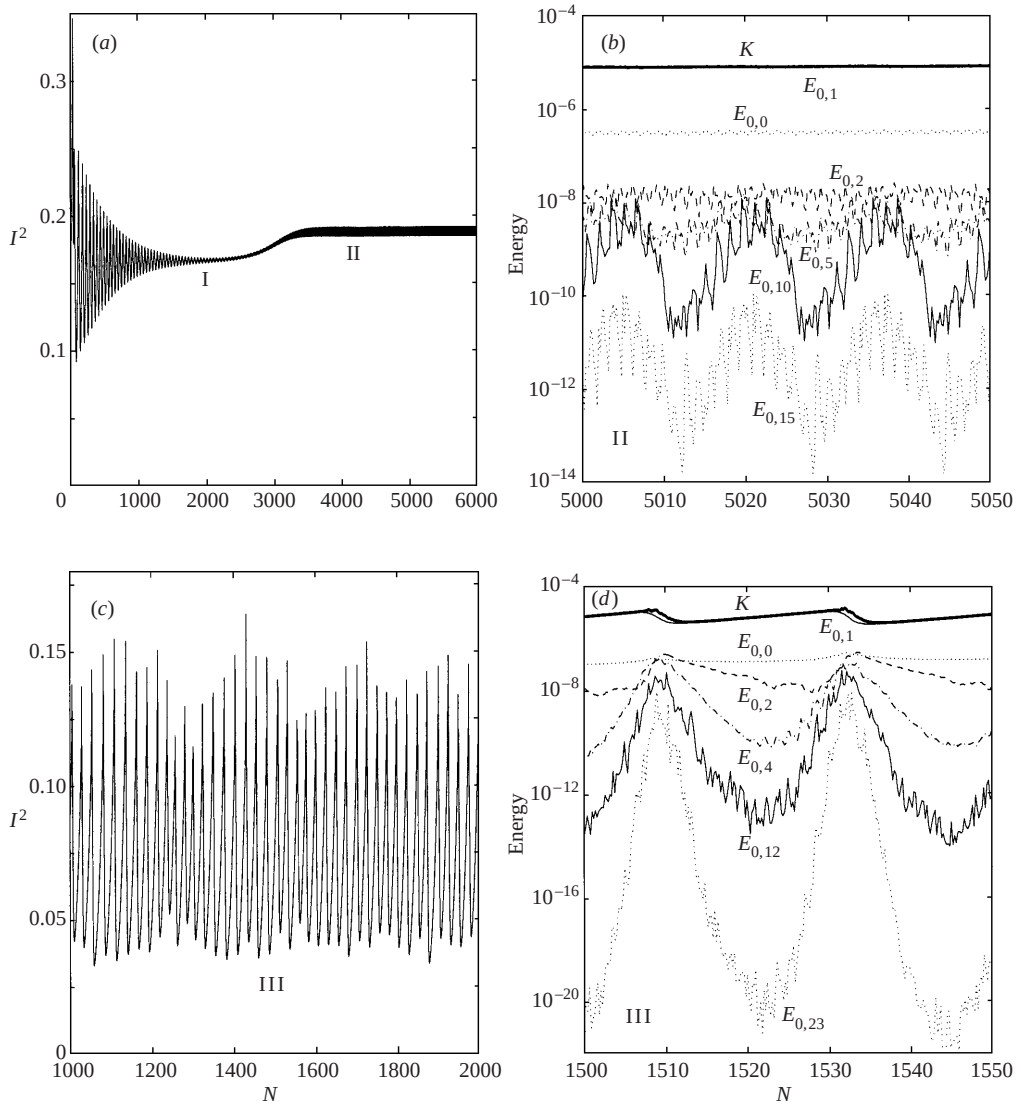

FIGURE 7. Weakly precessing case: $E = 10^{-5}$. Time series of intensity and energy distribution among the Fourier modes $E_{0,m}$. N is the number of fast revolutions. For (a) and (b) $\epsilon = 0.016$ $(N_y, N_z) = (16, 32)$. (a) Long time history of I^2. (b) Distribution of energy for branch II. K (thick solid line) is the total perturbation energy, and is indistinguishable from $E_{0,1}$. For (c) and (d) $\epsilon = 0.024$ $(N_y, N_z) = (24, 32)$. (c) Time series of I^2. (d) Distribution of energy for branch III.

dissipation is found to co-exist. At this value of ϵ different initial conditions can lead to either final state. Branch III was originally found at $\epsilon = 0.022$ and then traced back as far as $\epsilon = 0.0215$ by gradually decreasing ϵ. Below this value, the solution falls back down to branch II to complete a hysteretic cycle. On branch III at $\epsilon = 0.024$, the broadband nature of the frequencies present in the time series (figure 6c) indicates that this is a branch of chaotic solutions. The flow is now much more complex in both space and time (see figures 7c and 7d) and as a result requires at least $N_y = 24$ (runs at $N_y = 32$ were also done). The two data points corresponding to $\epsilon = 0.026$ and $\epsilon = 0.028$ appear to lie on a new fourth branch (IV). This is not overly clear from

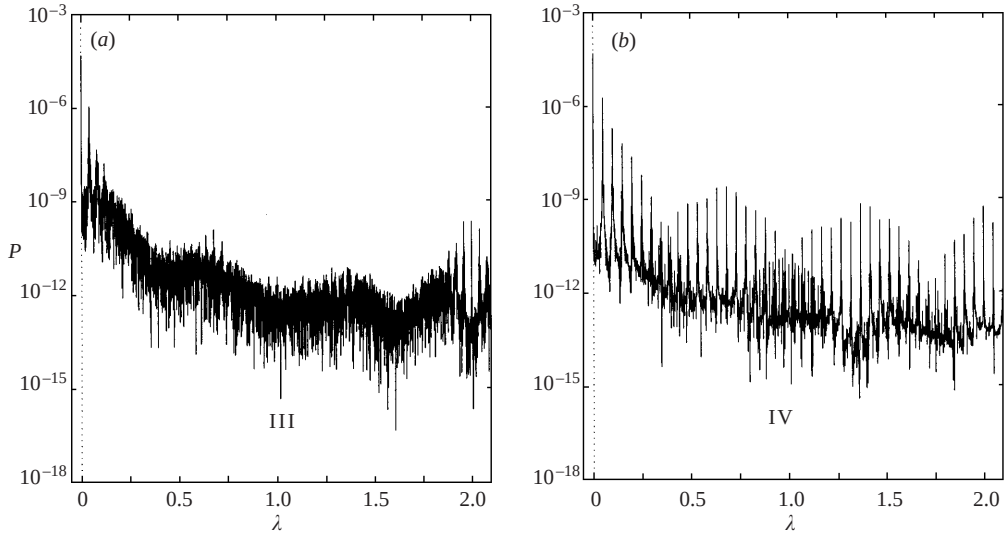

FIGURE 8. Weakly precessing case: $E = 10^{-5}$. Plots of the power spectra P against frequency λ for Fourier transforms of a (~ 1000 rev) time series of the perturbation energy K. (a) Branch III $\epsilon = 0.024$. (b) Branch IV $\epsilon = 0.028$.

comparing the $\tilde{w}$-time series at $\epsilon = 0.024$ and $\epsilon = 0.028$ (figures 6c and 6d which both contain broadband frequencies) but the emergence of a new periodicity at $\epsilon = 0.028$ is evident from the power spectra of their total energies (see figures 8a and 8b).

Further observations of figure 7 give us an insight into the energetic structure of the flow. In each of figures 7(b) and 7(d) we see a clear hierachy of energy levels associated with the Fourier modes $(0, m)$, which is a significant indication that we have enough resolution in the numerical experiments. Futhermore, we can see the increasing complexity of the flows as ϵ increases. In figure 7(d), for instance, the flow undergoes periods of relaxation and rapid transition, characterized by the variation of energy in the extremal mode (0, 23) over about 12 orders of magnitude. A final remark for each solution branch is that the majority of the energy is always associated with the linearly unstable mode. In particular, this implies that the mean flow (U_x, U_y) gives quite a small contribution to the overall flow.

The implications of this initial survey are clear. The primary bifurcation is supercritical and the flow disturbance quickly rises to attain an $O(1)$ value for I. The weakly nonlinear regime appears limited to an ϵ interval of size $O(\epsilon_{crit}^2)$ beyond $\epsilon = \epsilon_{crit}$. A secondary supercritical bifurcation emerges which then gives way to an abrupt transition to a higher and hence stronger chaotic branch. Even within this restricted two-dimensional setting, the flow dynamics are complicated, displaying multiple attracting solutions close ($\epsilon < 3\epsilon_{crit}$) to the bifurcation point.

Strongly precessing case: $E = 5 \times 10^{-5}$, $\epsilon \in [0.04996, 0.24]$

The precession rate was increased five-fold in order to accelerate the instability dynamics and shorten the necessary run times. Using the same type of initial conditions as above, four distinct solution branches, i–iv, were again found by an initial survey over precession rates $\epsilon \in [0.05, 0.24]$ (see figures 9 and 10). At these increased precession rates, the transitions between the branches were all found to be discontinuous. Once found, each branch was traced out by gradually adjusting the precession rate ϵ in steps of 0.001. Branch i corresponds to the saturated endstate of the two

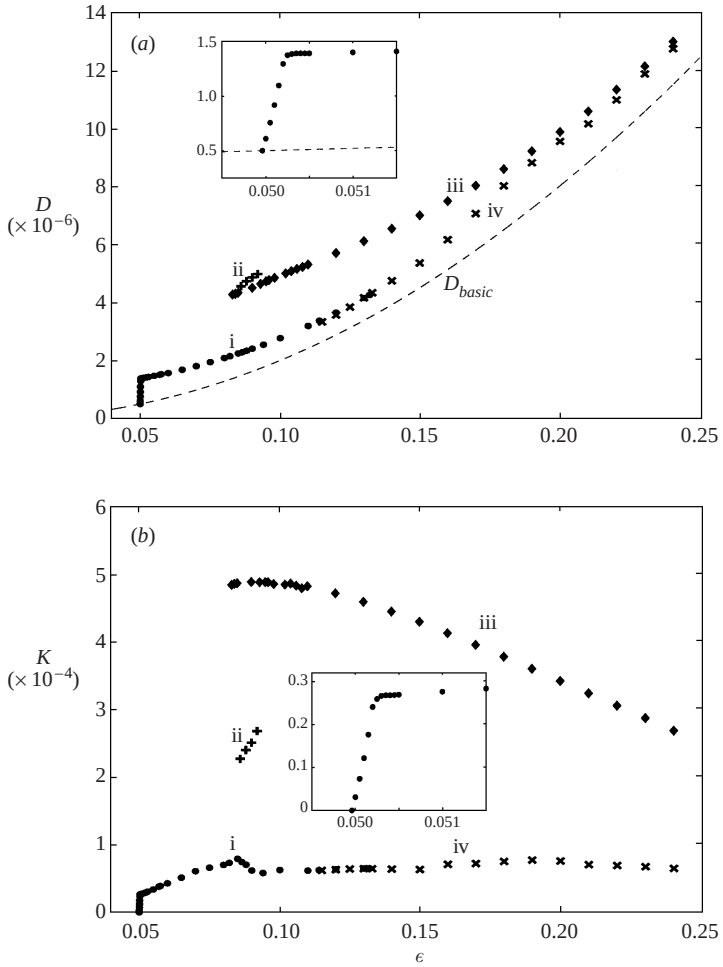

FIGURE 9. Strongly precessing case: $E = 5 \times 10^{-5}$. (*a*) Total dissipation D and (*b*) perturbation kinetic energy K for the solution branches, ●, i; +, ii; ◆, iii; ×, iv. The branches i, ii, iii and iv, exist on the ranges $0.04996 \leqslant \epsilon \leqslant 0.132$, $0.086 \leqslant \epsilon \leqslant 0.092$, $\epsilon \geqslant 0.083$ and $\epsilon \geqslant 0.115$, respectively.

growing inertial waves and extends from $\epsilon_{crit} = 0.04996$ to $\epsilon = 0.132$. Branch ii was found for $0.086 \leqslant \epsilon \leqslant 0.092$ and branch iii for $\epsilon \geqslant 0.083$. A final family of solutions corresponding to branch iv was found to exist for $\epsilon \geqslant 0.115$.

Figures 9 and 10 summarize how the energies and dissipation vary over the solution branches. Transitions found between the branches were as follows. If ϵ is decreased from 0.086 to 0.085 on branch ii, or from 0.083 to 0.082 on branch iii, the solution evolves to branch i. If ϵ is increased from 0.092 to 0.093 on branch ii, the solution evolves (restabilizes?) to branch iii and branch i leads to branch iv at $\epsilon = 0.133$ and vice versa at $\epsilon = 0.114$. (In all cases, the stability of a state was judged by eye after running for 6000 fast revolutions.) Various truncation levels of $N_y = 8, 16, 24$ and 32 were used to verify all the results.

As in the weakly precessing case, the initial bifurcation beyond $\epsilon = \epsilon_{crit}$ can be seen to be supercritical (subplot of figure 9), and following the analysis of that section we can estimate $\beta \approx 0.34$ which is in good agreement with the previous estimate.

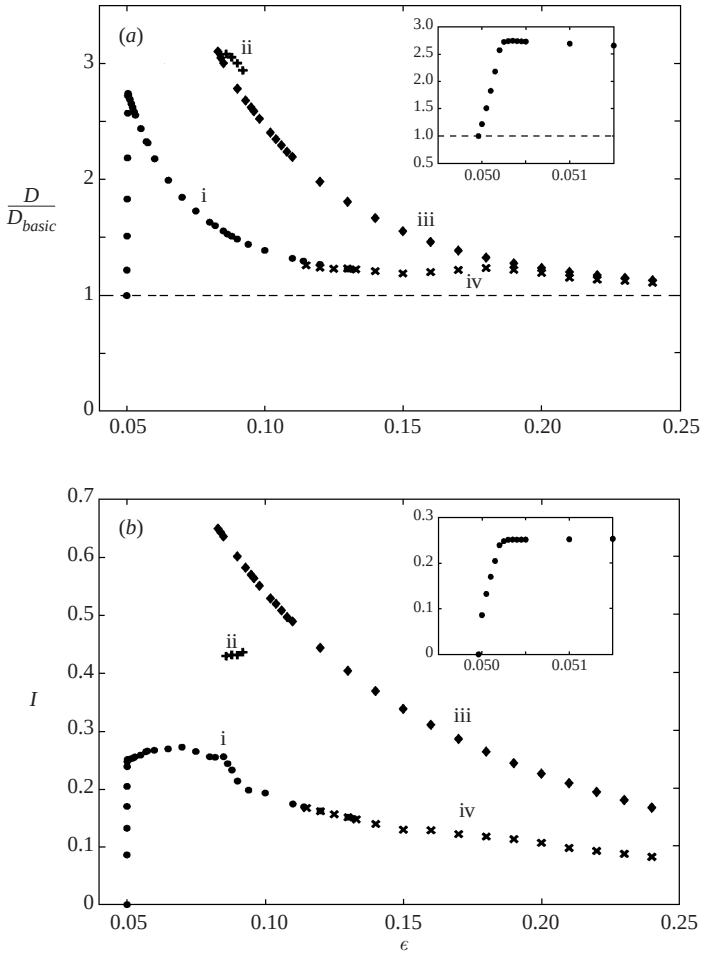

FIGURE 10. Strongly precessing case: $E = 5 \times 10^{-5}$. (a) Ratio of dissipation D to D_{basic} and (b) intensity I, for the four solution branches i to iv. The subplots show zooms of the initial bifurcation at $\epsilon \gtrsim \epsilon_{crit}$.

This adds weight to our previous (tentative) assertion that the ϵ-interval over which weakly nonlinear theory is valid is only $O(\epsilon_{crit}^2)$ beyond $\epsilon = \epsilon_{crit}$.

The power spectra in figure 11(a) confirm that branch i is the saturated nonlinear state of the two inertial waves, whose frequencies at $-\lambda_A = 0.3428$ and $\lambda_B = 0.6572$ are clearly visible. Figures 11(b) and (c), however, indicate that solution branches ii and iii represent very different types of solutions where discrete inertial wave frequencies are absent. Instead, the dominating frequencies are integer multiples of the basic state frequency $\lambda = 1$. The similarity between these figures and the additional frequencies present in figure 11(b) suggests that branch ii may represent solutions which have bifurcated from those on branch iii through a low-frequency instability (see also the time series shown in figure 12b, c). A typical power spectrum for branch iv (figure 11d) is essentially the power spectrum for branch i with a chaotic modulation added.

Figure 12 provides good insight into the energetic structure of the four solution branches. Branch i (figure 12a) has a very clearly ordered structure of energy within the Fourier modes, and likewise for branch iii (figure 12c). Figure 12(b), corresponding

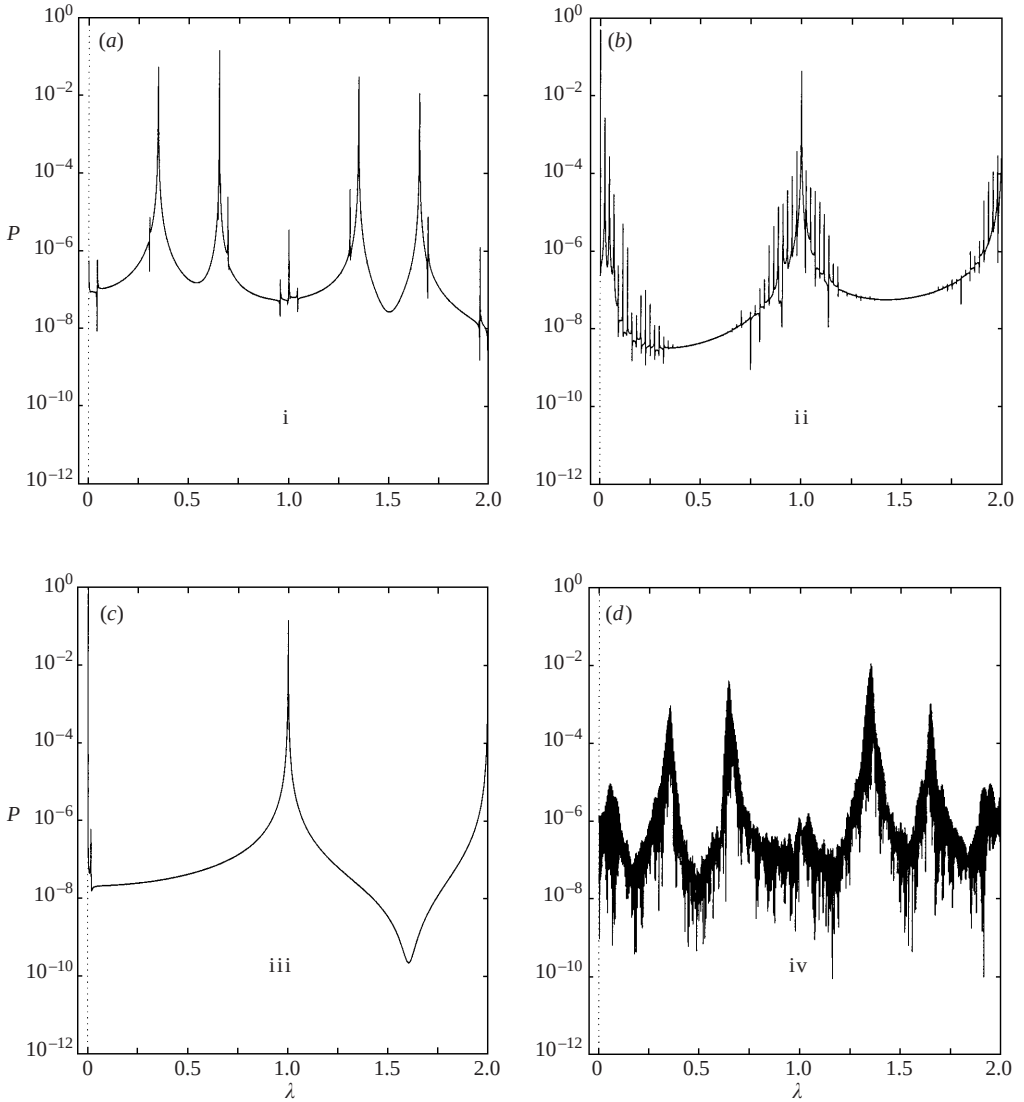

FIGURE 11. Strongly precessing case: $E = 5 \times 10^{-5}$. Power spectra P for the branches i to iv. All solutions produced with $(N_y, N_z) = (8, 32)$ except (d) which has $N_y = 16$. (a) Branch i solution for $\epsilon = 0.09$ and $t > 1500$ rev. (b) Branch ii solution for $\epsilon = 0.09$ and $t > 1000$ rev. (c) Branch iii solution for $\epsilon = 0.09$ and $t > 1000$ rev. (d) Branch iv solution for $\epsilon = 0.14$ and $t > 1000$ rev.

to branch ii has a similar energetic structure to branch iii on average, but a steady period of approximately 44 revolutions is also clearly evident (and corresponds to the additional slow frequency in figure 11*b*). Figure 12(*d*) indicates large temporal varitions in branch iv, as the solutions have periods where only the first modes (0,0) and (0,1) hold significant energy, followed by intervals where higher wavenumber Fourier modes play a significant role. A final point to note from each plot in figure 12 is that in all of these four branches the Fourier mode (0,0), i.e. the mean flow, contains the most energy for the majority of the time, even though the linear instability is present in the (0,1) mode. This is in contrast to the weakly precessing case, where (0,1) maintains the major share of the energy (figure 7*b*, *d*).

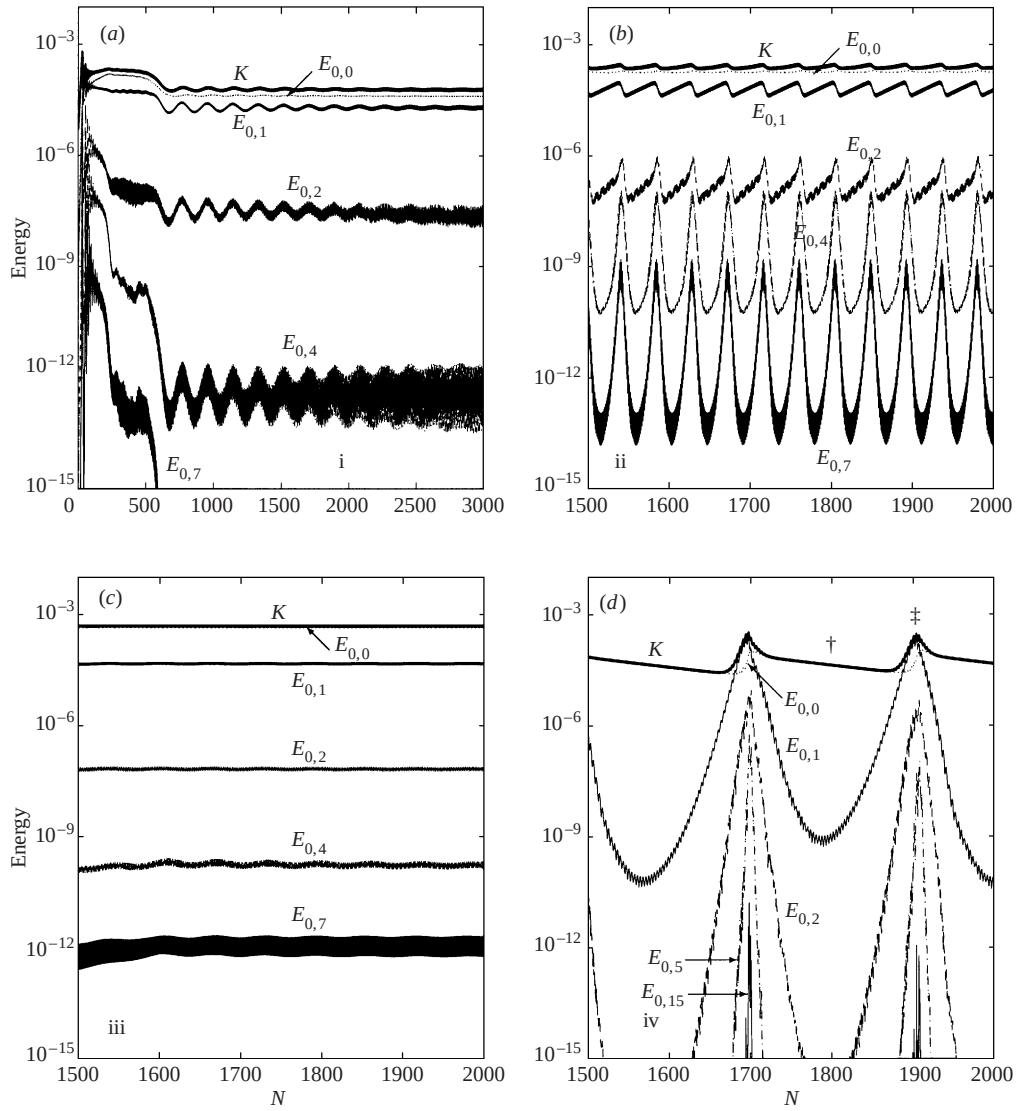

FIGURE 12. Strongly precessing case: $E = 5 \times 10^{-5}$. Time series of energy distribution among the Fourier modes $E_{0,m}$ for branches i to iv. K (thick solid line) is the total energy and N is the number of fast revolutions. (a) Branch i solution for $\epsilon = 0.09$. $E_{0,7}$ tends to 10^{-18} at long times. (b) Branch ii solution for $\epsilon = 0.09$. (c) Branch iii solution for $\epsilon = 0.09$. (d) Branch iv solution for $\epsilon = 0.14$. $E_{0,5}$ oscillates between 10^{-6} and 10^{-24} and $E_{0,15}$ between 10^{-11} and 10^{-40}. The markers † and ‡ refer to figure 14.

The same general features emerge as in the slowly precessing case above. The total dissipation increases with precession rate, whereas I tends to decrease so that the instability appears to become more 'efficient' in dissipating energy. There are again multiple attracting solutions for a given precession rate. For example, attracting solutions on branches i, ii and iii co-exist for $0.086 \leqslant \epsilon \leqslant 0.092$, and solutions on branches i, iii and iv for $0.115 \leqslant \epsilon \leqslant 0.132$. The 'strong' precession rate has, however, produced new types of solution given by branches ii and iii. Branch iii is particularly interesting since it represents a directly forced type of solution as the only frequencies

present are multiples of the fast precessional perturbation. Although its existence is perhaps not surprising, this solution can only exist as a finite-amplitude perturbation of the basic laminar state (branch iii cannot connect to the laminar state). Since figure 12(*c*) shows a steep drop off in the spectral energy with wavenumber, it seemed possible that a simple model of the solution could be isolated using only the mean and first harmonic. Numerical experiments confirmed that the solution could be captured comfortably with the severe truncation $N_y = 1$, but the complicated time-dependent z-structure of the velocity field thwarted any further reduction to a lower dimensional system.

Figures 13 and 14 show snapshots of u, $\tilde{u} = u - u_{basic}$ and w on the various branch solutions at times $t = 2\pi M + \frac{1}{6}\pi$ (so $u_{basic} = -2\epsilon z \sin t = -\epsilon z$) where M is chosen so that the branch of interest can be considered as stable. These allow us to visualize many of our previous observations for the velocity field. In particular, given any set of snapshots (a given row of figure 13 or 14) the leftmost plot, shows us how distorted the underlying shear flow of the basic state is by the perturbation velocity $\tilde{\boldsymbol{u}}$. Together with the centre plot, we can establish the relative contributions of the basic and perturbation velocities to the field as a whole. For example, in figure 13, the basic and perturbation velocities are always comparable (agreeing with our observation of flows with $I = O(1)$), whereas for the first row of figure 14 there is an order of magnitude separation between the contributions. Finally, comparisons of the central and rightmost plots give an indication of the contribution made by the mean flow, since this cannot play any part in the w component of the flow. Flows with a strong $\tilde{u}$ component and a weak $\tilde{w} = w$ component are therefore suggestive of a large mean flow, e.g. the first row of figure 14.

Other significant observations from figure 13 include the fact that branch i (figure 13*a–c*) clearly possesses the signature of the two inertial waves through the z-structure. Also the similarity of the velocity structures seen in figures 13(*d–f*) and 13(*g–i*) emphasizes the close relationship between branch ii and iii solutions. Figure 14 displays the branch iv solution at two different instances as it varies so much over one of its cycles (see figure 12*d*). In periods of relaxation (subplots (*a*)–(*c*)), the flow is dominated by the basic state $\boldsymbol{u}_{basic}$ and the main contribution to the perturbation velocity comes from the mean flow. However, only 60 revolutions later (see figure 12*d*), in periods of rapid transition the flow has $I = O(1)$ (w, for example, is nearly 30 times larger in (*f*) than in (*c*)), and the mean flow no longer dominates. We also observe that plots (*d*)–(*f*) have finer scales than those of (*a*)–(*c*).

5.2. *Three-dimensional nonlinear results*

The first decision in extending the numerical simulations to three dimensions was what wavenumber grid to take. Making the obvious choice $k_x = k_y = k_\perp$ would mean that two 'primary' instabilities would be simultaneously excited at $(k_x, k_y) = (k_\perp, 0)$ and $(0, k_\perp)$ making comparison with the two-dimensional results impossible. To avoid this, $k_x = \frac{2}{3}k_y$ was chosen throughout. The second decision was how to prescribe initial conditions. For general three-dimensional runs, the initial conditions for the two-dimensional runs – the Floquet eigenfunction at $(l, m) = (0, 1)$ with energy $E_{01} = 0.5 \times 10^{-5}$ – was augmented by adding random perturbations into Fourier mode locations $(l, m) = (0, 0)$, $l = 0, 2 \leqslant m \leqslant 4$ and $1 \leqslant l \leqslant 4, -4 \leqslant m \leqslant 4$ such that $E_{lm} = 0.5 \times 10^{-6}$ for these positions (the truncation used was always at least $(N_x, N_y, N_z) = (8, 8, 32)$). Using this over the range $0.05 \leqslant \epsilon \leqslant 0.24$ revealed the presence of three branches (A, B and C) of new three-dimensional solutions characterized by their dissipation and kinetic energy, as shown in figures 15 and 16.

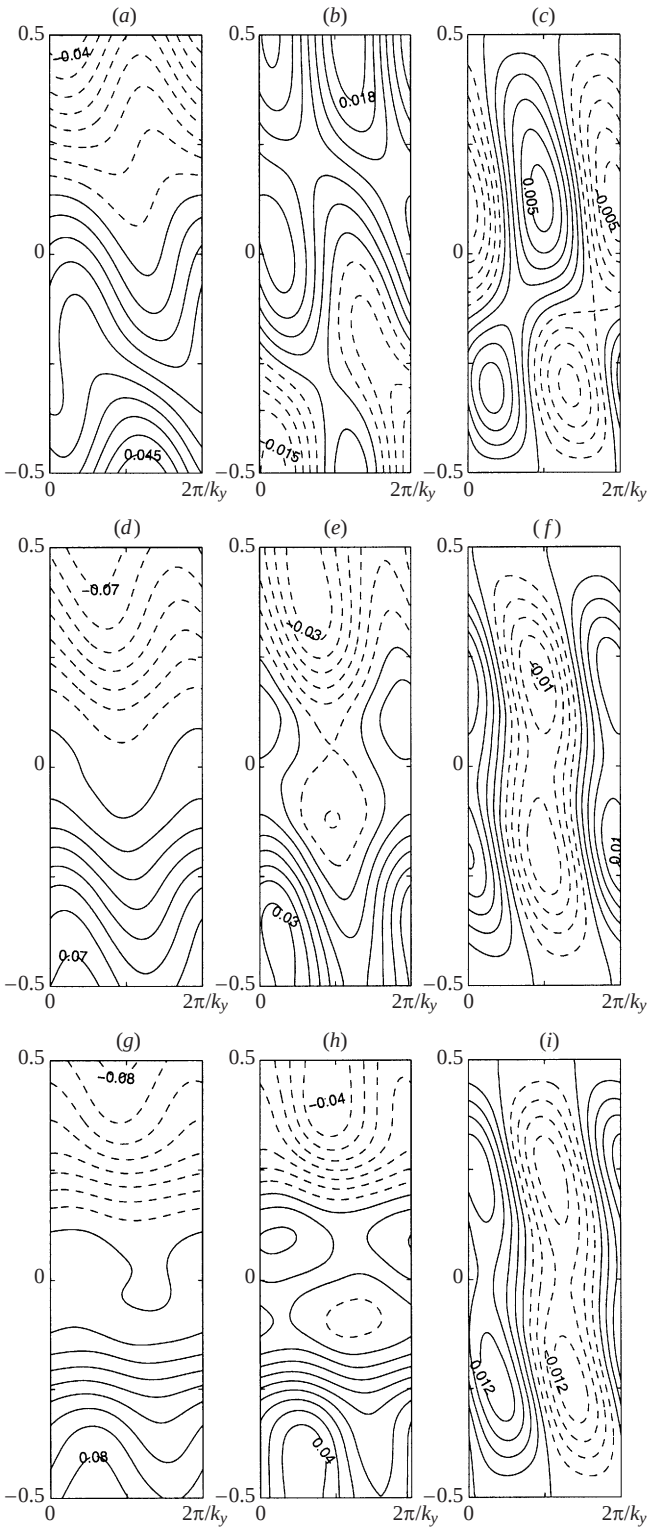

FIGURE 13. For caption see facing page.

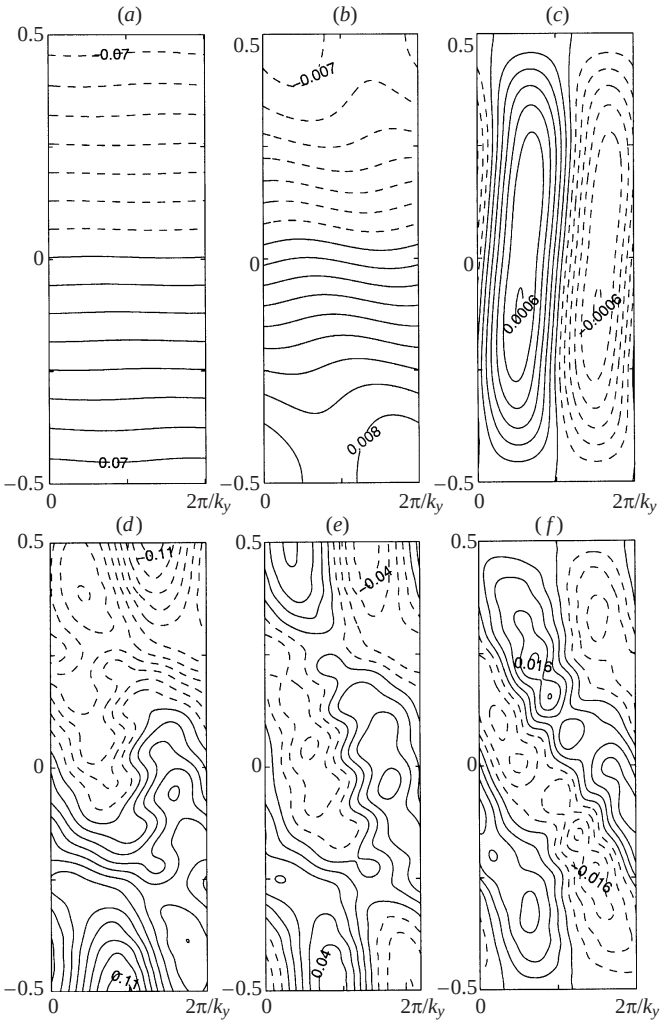

FIGURE 14. Strongly precessing case: $E = 5 \times 10^{-5}$. Eigenfunctions for the branch iv solution at $\epsilon = 0.14$. The contours in (*a*), (*b*) and (*c*) have equally spaced intervals of 0.01, 0.001 and 0.0001, respectively, and correspond to a snapshot at the point marked † on figure 12(*d*), where the flow is in a period of relaxation. The contours (*d*), (*e*) and (*f*) (with equally spaced intervals of 0.01, 0.01 and 0.004) but now at the point marked ‡ on figure 12(*d*) where the solution undergoes a period of rapid transition.

An interesting first observation is that branches B and C have much larger dissipations that any two-dimensional solutions at larger values of ϵ (figures 15*a* and 16*a*). These three-dimensional runs never selected any of the previously isolated two-dimensional states. All of the four branches of two-dimensional solutions were then tested for

FIGURE 13. Strongly precessing case: $E = 5 \times 10^{-5}$. Contour plots of the velocity field. In this and all subsequent contour plots the solid lines represent contour lines with values $\geqslant 0$ and the dotted lines < 0. Maxima and minima of the contour vales are given on each subplot. Plots (*a*), (*b*) and (*c*) show u, $u - u_{basic}$ and w, respectively, for the branch i solution at $\epsilon = 0.09$ where $\boldsymbol{u} = (u, v, w)$ is the velocity field. The contours have equally spaced intervals of 0.005, 0.003 and 0.001, respectively. Plots (*d*), (*e*) and (*f*) show likewise for the branch ii solution at $\epsilon = 0.09$. The contour separations are 0.01, 0.005 and 0.002. Plots (*g*), (*h*) and (*i*) are for branch iii at $\epsilon = 0.09$, with contour intervals 0.01, 0.005 and 0.003.

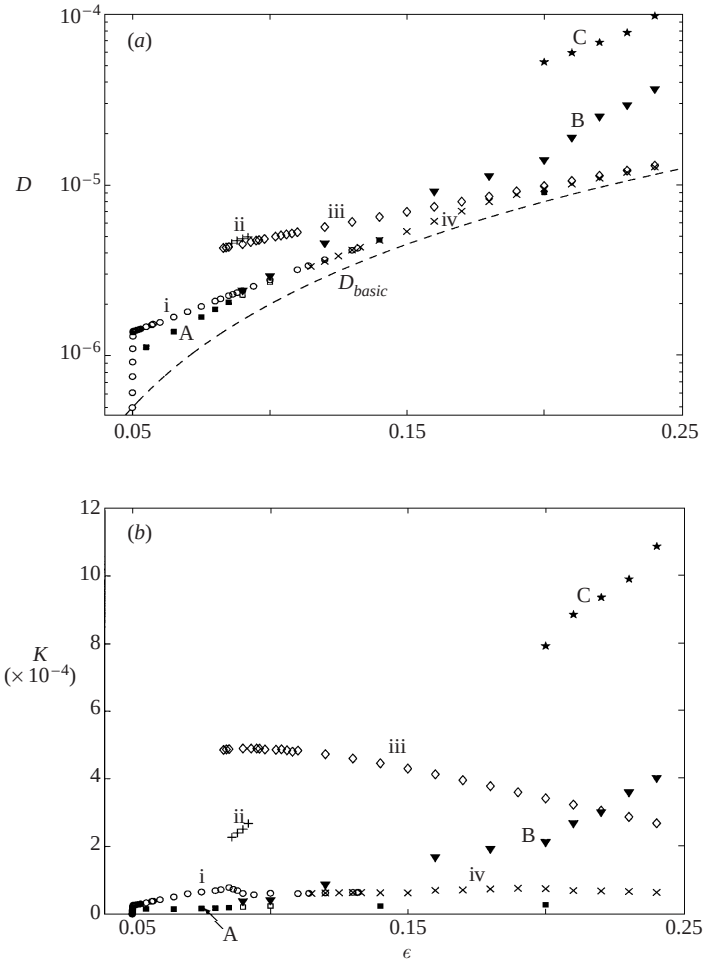

FIGURE 15. Three-dimensional strongly precessing case: $E = 5 \times 10^{-5}$, $\epsilon \in [0.05, 0.24]$. (*a*) Total dissipation D (note log scale) and (*b*) perturbation kinetic energy K for the solution branches, ■, A; ▼, B; ★, C. All two-dimensional (i to iv) branches are now unstable and are plotted with hollow/thin symbols.

three-dimensional stability and found to be linearly unstable. Branches A, B and C are found to exist for $0.04996 \leqslant \epsilon \leqslant 0.2$, $\epsilon \geqslant 0.09$ and $\epsilon \geqslant 0.2$, respectively.

The presence of the first three-dimensional branch (branch A) at low values of ϵ indicates that the two-dimensional branch i becomes three-dimensionally unstable very soon after criticality and certainly before becoming two-dimensionally unstable. This, of course, further restricts the use of weakly nonlinear theory. Surprisingly, branch A solutions are less dissipative than the co-existing two-dimensional state. A run at $\epsilon = 0.09$ shows the emergence of a new branch B through a continuous bifurcation. Figure 17 shows how initially the run traces a branch A-like solution for times less than 1500 rev but then evolves to a more energetic state – branch B. The inserts in figure 17 show how the frequencies differ between these two branches. Both early (branch A) and late (branch B) power spectra show that the flows are disordered, but certain frequencies resembling the primary inertial frequencies still appear to dominate. Branch B, however, also has two new frequencies of approximately 0.5 and

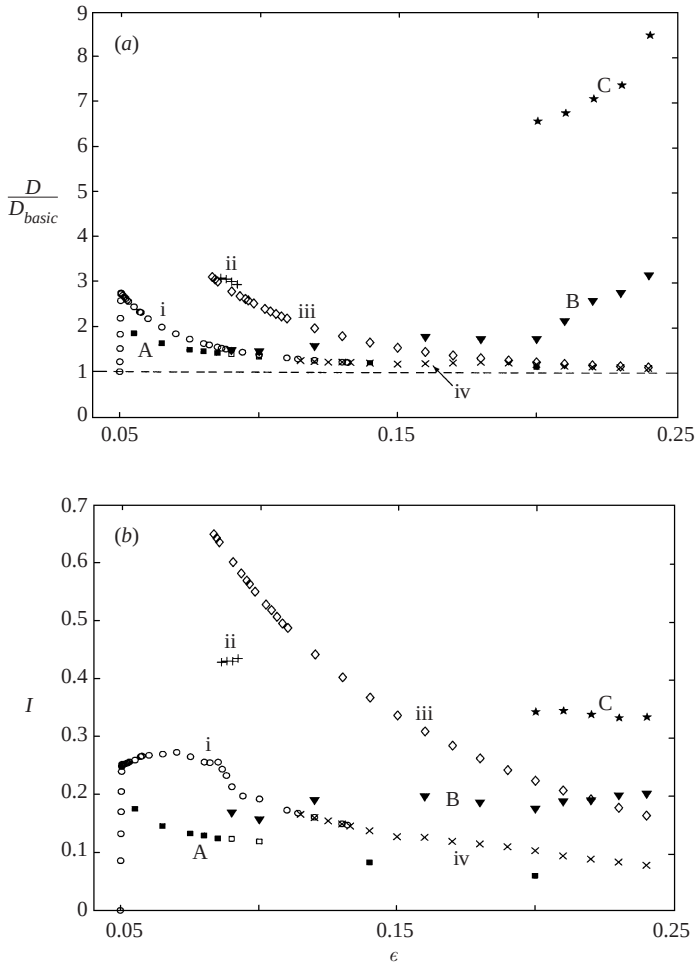

FIGURE 16. Three-dimensional strongly precessing case: $E = 5 \times 10^{-5}$, $\epsilon \in [0.05, 0.24]$. (*a*) Ratio of dissipation D to D_{basic} and (*b*) intensity I, for the three solution branches A to C. The unstable two-dimensional branches i to iv are also shown for reference.

1.5. A run at $\epsilon = 0.12$ traces out a more energetic version of the branch B state found at $\epsilon = 0.09$, but unexpectedly a run at $\epsilon = 0.14$ leads to a stable state clearly identifiable as being on branch A by its power spectrum. Runs at $\epsilon = 0.16$ and 0.18 lead to stable branch B solutions.

At $\epsilon = 0.20$, a new branch C of considerably enhanced dissipation is found to co-exist with branch A and B states. Figure 18 shows the time series and associated power spectra inserts for a long $(N_x, N_y) = (8, 8)$ run where it can be seen that the solution jumps abruptly between the three states at seemingly random times. In terms of intensity, the different states are clearly ordered as A, B, C with C being most intense. In terms of frequencies, the branches can also be clearly distinguished: A has the inertial frequencies with a chaotic modulation, B has extra peaks at approximately $\lambda = 0.5$ and $\lambda = 1.5$ and is more broadband, whereas C has its main peaks at frequencies of 0.5 and integer multiples thereof, although again the frequencies are largely broadband. Further runs using $(N_x, N_y) = (12, 12)$ and $(16, 16)$ confirm this behaviour with both showing exactly similar branch states and transitions although

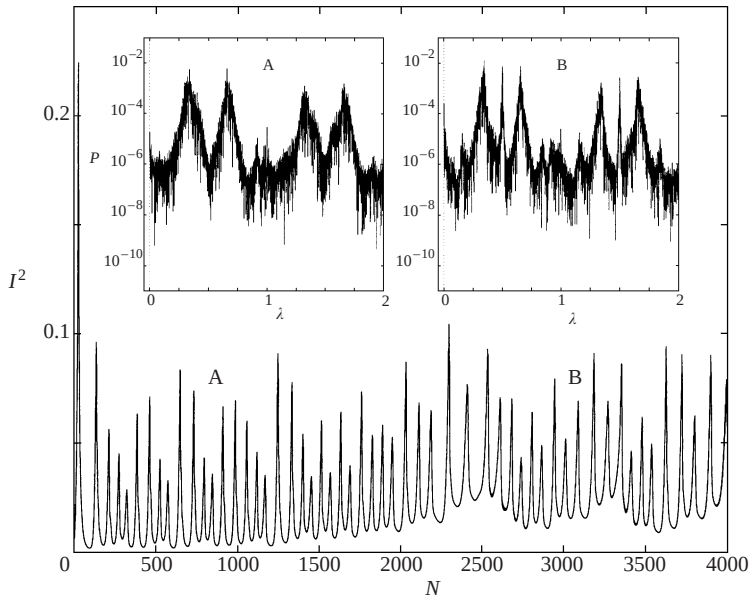

FIGURE 17. Three-dimensional strongly precessing case: $E = 5 \times 10^{-5}$. Time history of intensity squared (I^2) against number of revolutions, N, for $\epsilon = 0.09$ and $(N_x, N_y, N_z) = (8, 8, 32)$. The subplots A and B show the power spectra against frequencies for Fourier transforms over the intervals $100 \leqslant N \leqslant 1500$ and $N \geqslant 2200$, respectively.

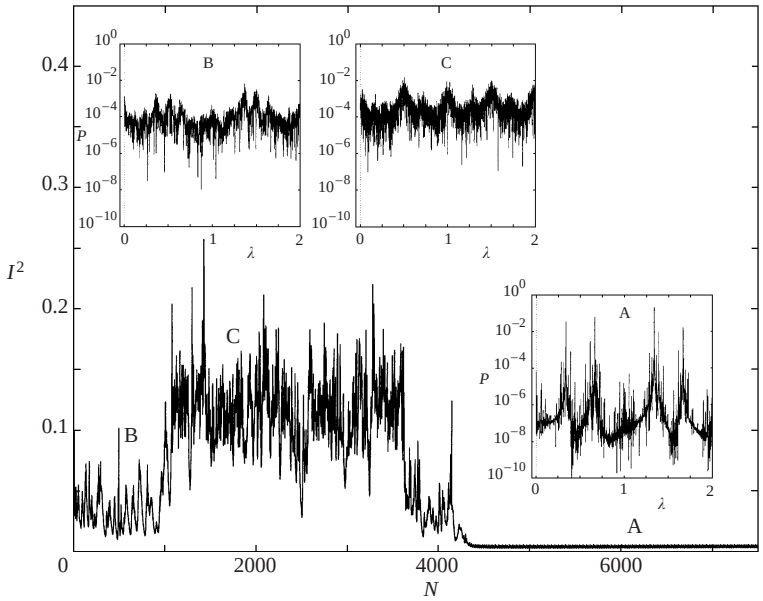

FIGURE 18. Three-dimensional strongly precessing case: $E = 5 \times 10^{-5}$. Time history of intensity squared (I^2) against number of revolutions, N, for $\epsilon = 0.2$ and $(N_x, N_y, N_z) = (8, 8, 32)$. The subplots show the power spectra for each of the branches A to C.

the points of transition, of course, occurred at differing times. Runs for $\epsilon > 0.20$ show exactly the same type of behaviour except a branch A state is not now seen. Figure 19 shows a typical time series for $\epsilon = 0.24$ where there is chaotic switching between branches B and C of the flow solution. These switches are sometimes very

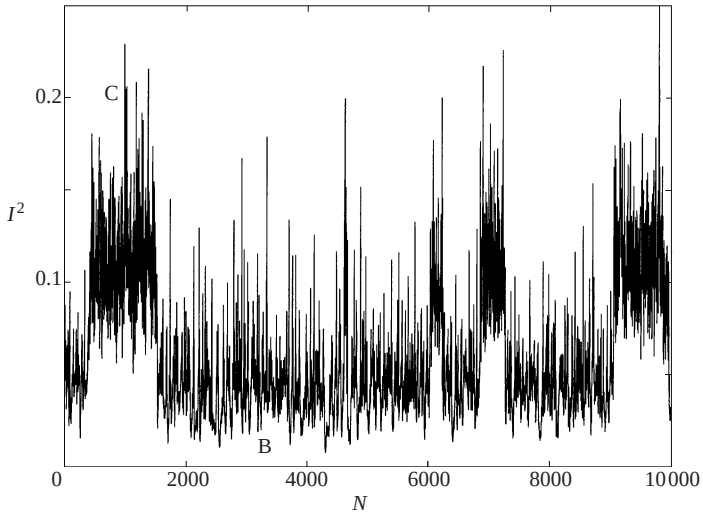

FIGURE 19. Three-dimensional strongly precessing case: $E = 5 \times 10^{-5}$. Long time history of intensity squared (I^2) against number of revolutions, N, for $\epsilon = 0.24$ and $(N_x, N_y, N_z) = (8, 8, 32)$.

short lived (for example the apparent change to branch C at approximately 4650 rev) which only last for a few tens of revolutions and sometimes very pronounced (for example the persistence of branch B from approximately 1500 to 4600 rev).

Figure 20 shows snapshots of the solutions on branches A, B and C for $\epsilon = 0.20$. Time is such that the basic state velocity component u_{basic} has a form $\epsilon z = 0.2z$, and is therefore bounded by ± 0.1. The velocity deviation $\tilde{\boldsymbol{u}}$ can be seen to both increase in magnitude and spatial complexity in going from branch A to branch C. For branch A (subplots (a) and (b)) the inertial wave structure in the y-direction can be seen in subplot (b) and generally the perturbation flows are small (10 to 20 times smaller) compared to the basic state. For branch B (subplots (c) and (d)) the perturbation flows are again small (5 to 10 times smaller) than the basic state, but not as small as for branch A. For branch C (subplots (e) and (f)) the perturbation flows are now only 2 to 4 times smaller than the basic state. These observations are entirely consistent with increasing intensity I in moving from branches A to C. We also observe that branch C exhibits finer scales in both x and y than both B and (certainly) A. A final point to note is that for branch A, the velocities $\tilde{u}$ and $\tilde{w}$ are comparable in size, whereas $\tilde{u}$ is typically a factor of 2 larger than $\tilde{w}$ for branches B and C. This indicates an increased role of the mean flow in the more energetic states B and C.

The increased spatial and temporal complexity of three-dimensional flows raises important issues of numerical resolution. The smoothness of the contours in figures 20(a)–20(d) indicates that the solution branches A and B are well resolved whereas the situation is less clear for branch C (figure 20e, f). In figure 21, the coefficients e_{lmn} and U_{xn} defined in equations (3.4) and (3.6) are plotted against the Chebyshev index n, for two different levels of truncation $N_z = 32$ and 48 for branch A and C-type solutions. The solutions for $N_z = 48$ were found by taking an initial condition from $N_z = 32$, increasing the truncation, and allowing the solution to evolve over 175 revolutions. Since the spectral decompositions are taken at different times we expect the coefficients for a given expansion polynomial to be different, but follow the same general trend as the polynomial index n increases. Figure 21 confirms this for both branches. This, together with the observation that similar behaviours are

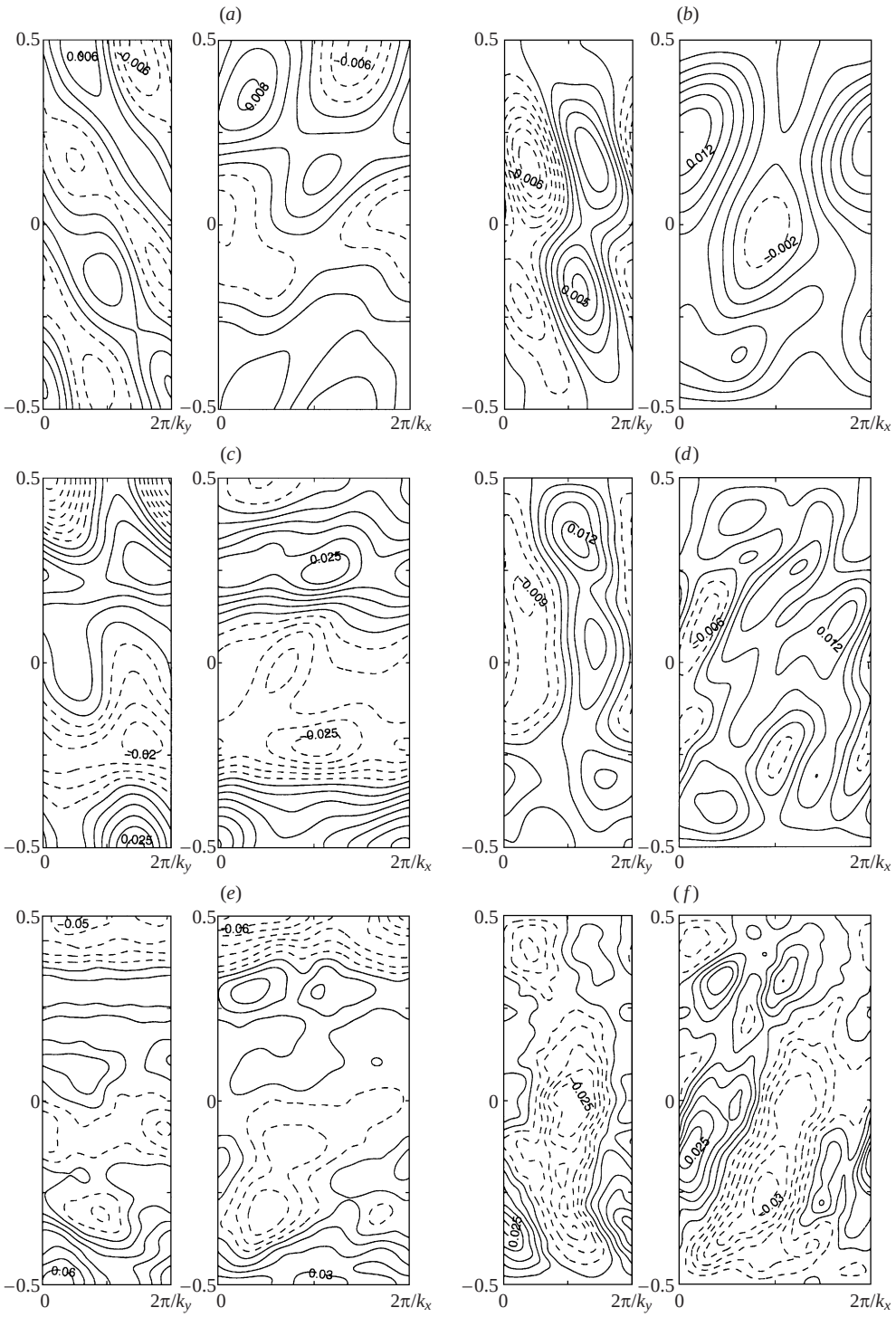

FIGURE 20. For caption see facing page.

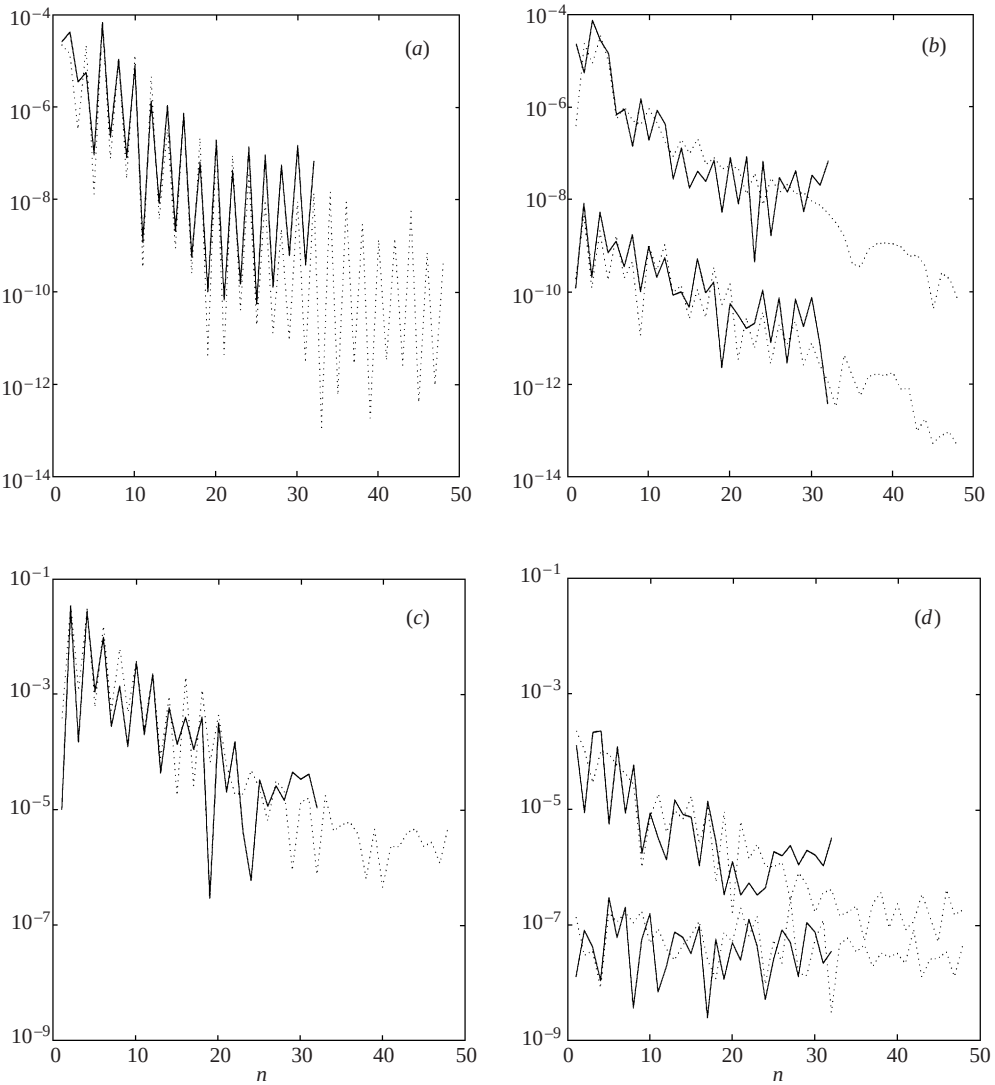

FIGURE 21. Spectral decompositions of some representative Fourier modes for branch A – plots (*a*) and (*b*), and branch C – plots (*c*) and (*d*) – solutions. All solutions calculated with $(N_x, N_y) = (8, 8)$ and $\epsilon = 0.2$. The solid lines give a decomposition for $N_z = 32$, and the dotted lines for $N_z = 48$. Plots (*a*) and (*c*) are the coefficents of ϕ_n in the expansion (3.6) for U_x. Plots (*b*) and (*d*) give the real part of the coefficients of ϕ_n in the expansion (3.4) for e, where the upper lines are for the Fourier mode $(l, m) = (0, 1)$ and the lower lines for $(l, m) = (4, 4)$.

FIGURE 20. Snapshots in the three-dimensional strongly precessing case: $E = 5 \times 10^{-5}$. The subplots are organised into pairs where the left-hand (narrow) plot is a given quantity in the (y, z)-plane taken as a slice in three-dimensional space at $x = \sqrt{2}\,\pi/k_x$, and the right-hand (wider) plot is the same quantity in the (x, z)-plane taken as a slice in three-dimensional space at $y = \sqrt{2}\,\pi/k_y$. (*a*) and (*b*) show $\tilde{u}$ and $\tilde{w}$ for the branch A solution at $\epsilon = 0.2$ and correspond to a time near 5000 rev from figure 18. (*c*) and (*d*) show likewise for branch B at $\epsilon = 0.2$ corresponding to a time near 200 rev from figure 18, and (*e*) and (*f*) are for branch C at $\epsilon = 0.2$ corresponding to a time near 3000 rev from figure 18. Contour separations are from top-left to bottom-right 0.002, 0.002, 0.001, 0.002, 0.005, 0.005, 0.003, 0.003, 0.01, 0.01, 0.005 and 0.005.

found for increases in N_x and N_y, is an excellent indication that a truncation level of $N_z = 32$ leads to sufficiently resolved velocity fields for all the branches.

The branch-switching dynamics is the new feature to emerge from the three-dimensional simulations. The clear implication is that precessing flows can exhibit (chaotic) dynamics over time scales completely unrelated with the fast 'driving' frequency. It is also significant that the three-dimensional solutions represent highly dissipative states (branch C) as is the fact that these states are and remain strong instabilities: figure 16(b) shows that $I = O(1)$. In general terms, as in the two-dimensional cases, the selected flows become more efficient in dissipating energy; the strength of the instability remains fairly constant, but the dissipation still increases as $\epsilon - \epsilon_{crit}$ increases.

6. Discussion

The results presented in this paper have revealed the presence of rich nonlinear dynamics in a precessing fluid layer. In the particular situations studied (stress-free boundary conditions and the two ranges of precession rates $\epsilon \in [0.09885, 0.028]$ and $\epsilon \in [0.04996, 0.24]$), we have found the co-existence of multiple nonlinear states, some of which are chaotic, and chaotic branch-switching all relatively close to criticality ($\epsilon < 5\epsilon_{crit}$). Even at the lower (weak) precession rate range, discontinuous bifurcations and chaotic states have been found. The general trend seems to be for the flow to select the most 'efficient' dissipative state available to it where 'efficiency' has been loosely defined as some ratio of total dissipation to instability kinetic energy. Discontinuous bifurcations to chaotic solutions lead to a jump in this efficiency. The fact that no nonlinear state has been observed here for $\epsilon \leqslant \epsilon_{crit}$ tends to suggest that the precessional instability is strictly supercritical. Estimates of the threshold for instability based upon balancing growth rates with inertial wave viscous decay rates then provide an accurate indication of when the simple basic flow response may not be realized.

We have found that weakly nonlinear theory is at best valid only in a small $O(\epsilon_{crit}^2)$ interval beyond $\epsilon = \epsilon_{crit}$. This was found numerically by seeing when the two-dimensional solution branch no longer increased like $(\epsilon - \epsilon_{crit})^{1/2}$ away from the bifurcation point. This scaling may also be argued for on the basis that secondary instabilities will naturally tend to occur by this point. Two inertial waves can be expected to take part in a triad resonance with one of the finite amplitude primary waves if the amplitude of the primary inertial wave is of the same order as a typical viscous damping rate for a wave, that is $(\epsilon - \epsilon_{crit})^{1/2} \sim O(Ek^2) \sim O(\epsilon_{crit})$ (Kerswell 1999). This then recovers the same interval size of $O(\epsilon_{crit}^2)$.

One of the stated goals of this paper has been to explore the nonlinear dynamics of precessional instabilities beyond the secondary instability that is observed in the closely related 'elliptical' situation. In our two-dimensionally-restricted weakly precessing situation, $\epsilon \in [0.09885, 0.028]$, we have confirmed the presence of a supercritical secondary instability and found that the tertiary bifurcation is an abrupt transition to a chaotic attractor. This behaviour is in keeping with the Ruelle–Takens (1971) transition scenario although the final state appears only chaotic in time and therefore far from turbulent. In the strongly precessing case $\epsilon \in [0.04996, 0.24]$, the two-dimensional flow dynamics seems to switch directly from the primary branch (i) to a chaotic branch (iv) (branches ii and iii being coincidental). This is probably because the secondary and tertiary bifurcations occur so close together. Certainly, this seems

to be the case when the dynamics are allowed to be three-dimensional since the chaotic branch A exists very near to $\epsilon = \epsilon_{crit}$.

Given our limited data, the picture which has emerged is that the flow dynamics tend to assume a chaotic state at the tertiary bifurcation (the 'Ruelle–Takens' scenario) rather than follow a gradual increase in complexity as new frequencies are added through successive bifurcations (the 'Landau' scenario). This then poses the next question as to how these chaotic states change into turbulent states. Importantly, all the solutions found in this study remain within $O(\epsilon)$ (in the kinetic energy norm) of the basic state since I never exceeds 1. Hence, although these can be classed as 'strong' instabilities relative to 'weak' viscous instabilities where $I \ll 1$, it still remains the case that the nonlinear dynamics revealed here seem too weak to explain the most dramatic aspects of experimental observations. In the case of contained elliptical flows (Malkus 1989; Eloy *et al.* 2000, 2002), the flow can be seen to break down intermittently to small scales when the elliptical distortion is sufficiently large. These small scales then decay before the flow relaminarizes. In contrast, a strongly precessed oblate spheroid seems able to sustain a small-scale flow where the average rotation axis of the flow is changed completely (Malkus 1968). Both situations clearly indicate that I must reach values of $O(1/\epsilon)$ since the underlying rotation of the flow is either temporarily destroyed or tipped over into a new direction. This distinction is crucial as $I = O(1)$ indicates that the instability is only able to access the energy of the sheared flow whereas $I = O(1/\epsilon)$ implies that the sheared flow acts like a catalyst to release energy stored in the underlying rotation.

There seem to be four possibilities for why we have not observed these extreme solutions. First, and perhaps most likely, the system is not sufficiently nonlinear or supercritical. Experimental realizations are typically carried out far away from critical conditions so that things happen quickly and new flows are large enough to see. It is not unreasonable to imagine that the values of ϵ studied here are still not large enough compared to E to see this behaviour. Secondly, it has only been practical to study a simple form of three-dimensional instability in which one inertial instability is tuned in. This is an obvious starting point for a first study like this, but does exclude more complicated dynamics. Generically, if the precession rate is high enough, many primary instabilities will be simultaneously excited and we can imagine a more energetic flow response. However, it is pure speculation whether this would explain the discrepancy. Thirdly, the fact that I remains $O(1)$ may be an unfortunate feature of adopting a planar geometry. One of the key features of the experimental observations discussed above is the fact that the flow is seen to be appreciably despun at some points in time. Unfortunately, this is an inherently local (or bounded) phenomenon which cannot formally be captured in a planar model because the growing disturbance is forced to be spatially periodic, whereas the underlying rotation field is not. This is in some way compensated by allowing the presence of mean flows, but the fact remains that this is a notable weakness of using a planar unbounded geometry to model a physically bounded rotating system. Again, it is unclear whether this is really restricting the dynamics or not. Fourthly, some crucial physics important for the dramatic experimental observations may be absent from the study here. The presence of thin viscous shear and boundary layers is the most obvious omission, however, their instability seems so weak and localized; values of $I^2 = K_{inst}/K \leqslant 0.01$ have been reported (Lorenzani & Tilgner 2001; Tilgner & Busse 2001) compared to values in the range $(0.1 - 0.36)$ for the instabilities here (see figure 16*b*). This greater 'strength' of the inertial instabilities compared to the viscous instabilities as well as their global rather than local influence would seem to

make them favourite for the likely cause of the transition observed in a precessing oblate spheroid even though there is still this issue of reaching even larger values of I for the fully turbulent response.

The fact that the flow solution has been found to switch chaotically between different nonlinear states over long times seemingly unrelated to the fast precessional frequency is significant for the precessing Earth. The clear implication is that the precessional stirring of the Earth's core can produce 'events' over very much longer time scales than the daily period of the precessional effect. The next challenge, of course, is to understand how the flows described here are modified or suppressed in a precessing and convecting core. The plane layer model introduced here should prove a useful arena in which to explore this question. A further question for the future is whether the discovered chaotic flows could act as dynamos, that is, whether they could generate a magnetic field if the fluid were electrically conducting. After a period of cautious scepticism, the current consensus is that any sufficiently complicated, three-dimensional velocity field should work. However, this remains to be checked and, of course, also the character of the ensuing magnetic field clarified.

Finally, it is worth re-emphasizing that the complex nonlinear dynamics uncovered here for the precessing plane layer should be closely analogous with those present in an elliptical flow. Only the quantitative details of the linear instability mechanism differ between the two scenarios; qualitatively the instability mechanisms are identical (e.g. see Kerswell 2002). Beyond the initial flow dominated by the two growing inertial waves, other mechanisms such as the instability of finite-amplitude inertial waves (Fabijonas, Holm & Lifschitz 1997; Kerswell 1999) come into play, which should make the dynamics generic to strained rotating flows.

We are very grateful to Professor C. A. Jones for sharing his optimized fast Fourier transform routines and to one of the referees who offered many constructive criticisms which considerably improved this manuscript. Support from NERC (a studentship for R.M.M.) and The Royal Society (R.R.K.) is gratefully acknowledged.

REFERENCES

Barnes, D. R. & Kerswell, R. R. 2000 New results in rotating Hagen–Poiseuille flow. *J. Fluid Mech.* **417**, 103–126.

Busse, F. H. 1968 Steady fluid flow in a precessing spheroidal shell. *J. Fluid Mech.* **33**, 739–751.

Eloy, C., Le Gal, P. & Le Dizès, S. 2000 Experimental study of the multipolar vortex instability. *Phys. Rev. Lett.* **78**, 1900–1903.

Eloy, C., Le Gal, P. & Le Dizès, S. 2002 Elliptic and triangular instabilities in rotating cylinders. *J. Fluid Mech.* submitted.

Fabijonas, B., Holm, D. D. & Lifschitz, A. 1997 Secondary instabilities of flows with elliptic streamlines. *Phys. Rev. Lett.* **78**, 1900–1903.

Gans, R. F. 1970*a* On the precession of a resonant cylinder. *J. Fluid Mech.* **41**, 865–872.

Gans, R. F. 1970*b* On the hydromagnetic precession in a cylinder. *J. Fluid Mech.* **45**, 111–130.

Gledzer, E. B., Dolzhansky, F. V., Obukhov, A. M. & Ponomarev, V. M. 1975 An experimental and theoretical study of the stability of a liquid in an elliptical cylinder. *Isv. Atmos. Ocean. Phys.* **11**, 617–622.

Gledzer, E. B., Novibov, Y. V., Obukhov, A. M. & Chusov, M. A. 1974 An investigation of the stability of liquid flows in a three-axis ellipsoid. *Isv. Atmos. Ocean. Phys.* **10**, 69–71.

Greenspan, H. P. 1968 *The Theory of Rotating Fluids.* Cambridge University Press (reprinted Breukelen Press, Brookline 1990).

Hollerbach, R. & Kerswell, R. R. 1995 Oscillatory internal shear layers in rotating and precessing flows. *J. Fluid Mech.* **298**, 327–339.

Jones, C. A. & Roberts, P. H. 2000 Convection-driven dynamos in a rotating plane layer. *J. Fluid Mech.* **404**, 311–343.

Kerswell, R. R. 1993 The instability of precessing flow. *Geophys. Astrophys. Fluid Dyn.* **72**, 107–144.

Kerswell, R. R. 1994 Tidal excitation of hydromagnetic waves and their damping in the Earth. *J. Fluid Mech.* **274**, 219–241.

Kerswell, R. R. 1995 On the internal shear layers spawned by the critical regions of oscillatory Ekman boundary layers. *J. Fluid Mech.* **298**, 311–325.

Kerswell, R. R. 1999 Secondary instabilities in rapidly rotating flows: inertial wave breakdown. *J. Fluid Mech.* **382**, 283–306.

Kerswell, R. R. 2002 Elliptical instability. *Annu. Rev. Fluid. Mech.* **34**, 83–113.

Kerswell, R. R. & Malkus, W. V. R. 1998 Tidal instability as a source for Io's magnetic field signature. *Geophys. Res. Lett.* **25**, 603–606.

Kobine, J. J. 1995 Inertial wave dynamics in a rotating and precessing cylinder. *J. Fluid Mech.* **303**, 233–252.

Laporte, F. & Corjon, A. 2000 Direct numerical simulations of the elliptical instability of a vortex pair. *Phys. Fluids* **12**, 1016–1031.

Lorenzani, S. & Tilgner A. 2001 Fluid instabilities in precessing spheroidal cavities. *J. Fluid Mech.* **447**, 111–128.

Lungren, T. S. & Mansour, N. M. 1996 Transition to turbulence in an elliptical vortex. *J. Fluid Mech.* **307**, 43–62.

Mahalov, A. 1993 The instability of rotating fluid columns subjected to a weak external Coriolis force. *Phys. Fluids* **5**, 891–900.

Malkus, W. V. R. 1968 Precession of the Earth as a cause of geomagnetism. *Science* **169**, 259–264.

Malkus, W. V. R. 1989 An experimental study of the global instabilities due to the tidal (elliptical) distortion of a rotating elastic cylinder. *Geophys. Astrophys. Fluid Dyn.* **48**, 123–134.

Manasseh, R. 1992 Breakdown regimes of inertia waves in a precessing cylinder. *J. Fluid Mech.* **243**, 261–296.

Manasseh, R. 1994 Distortions of inertia waves in a rotating fluid cylinder forced near its fundamental mode resonance. *J. Fluid Mech.* **265**, 345–370.

Manasseh, R. 1996 Nonlinear behaviour of contained inertia waves. *J. Fluid Mech.* **315**, 151–173.

Mason, D. M. & Kerswell, R. R. 1999 Nonlinear evolution of the elliptical instability: an example of inertial wave breakdown. *J. Fluid Mech.* **396**, 73–108.

Moore, D. W. & Saffman, P. G. 1975 The instability of a straight vortex filament in a strain field. *Proc. R. Soc. Lond.* A **346**, 413–425.

Noir, J., Jault, D. & Cardin, P. 2001 Numerical study of the motions within a slowly precessing sphere at low Ekman number. *J. Fluid Mech.* **437**, 283–299.

Pais, M. A. & Le Mouel, J. L. 2001 Precession-induced flows in liquid-filled containers and the Earth's core. *Geophys. J. Intl* **144**, 539–554.

Perryman, M. A. C. 2000 Extra-solar planets. *Rep. Prog. Phys.* **63**, 1209–1272.

Poincaré, H. 1910 Sur la précession des corps déformables. *Bull. Astronomique* **27**, 321–356.

Rieutord, M. 2000 A note on inertial waves in the core of the Earth. *Phys. Earth Planet Inter. 117*, 63–70.

Roberts, P. H. & Stewartson, K. 1965 On the motion in a liquid in a spheroidal cavity of a precessing rigid body II. *Proc. Camb. Phil. Soc.* **61**, 279–288.

Ruelle, D. & Takens, F. 1971 On the nature of turbulence. *Commun. Math. Phys.* **20**, 167–192.

Seyed-Mahmoud, B., Henderson, G. & Aldridge, K. D. 2000 A numerical model for the elliptical instability of the Earth's fluid outer core. *Phys. Earth Planet Inter.* **117**, 51–61.

Showman, A. P. & Malhotra, R. 1999 The Galilean satellites, *Science* **286**, 77–84.

Stewartson, K. & Roberts, P. H. 1963 On the motion of a liquid in a spheroidal cavity of a precessing fluid body. *J. Fluid Mech.* **17**, 1–20.

Tilgner, A. 1999*a* Driven inertial oscillations in spherical shells. *Phys. Rev.* E **59**, 1789–1794.

Tilgner, A. 1999*b* Magnetohydrodynamic flow in precessing spherical shells. *J. Fluid Mech.* **379**, 303–318.

Tilgner, A. 1999*c* Non-axisymmetric shear layers in precessing fluid ellipsoidal shells. *Geophys. J. Intl* **136**, 629–636.

Tilgner, A. & Busse, F. H. 2001 Flows in precessing spherical shells. *J. Fluid Mech.* **426**, 387–396.

Vanyo, J. P. 1991 A geodynamo powered by luni-solar precession. *Geophys. Astrophys. Fluid Dyn.* **59**, 209–234.

Vanyo, J. P., Wilde, P., Cardin, P. & Olson, P. 1995 Experiments on precessing flows in the Earth's liquid-core. *Geophys. J. Intl* **121**, 136–142.

Vanyo, J. P. & Dunn, J. R. 2000 Core precession: flow structures and energy. *Geophys. J. Intl* **142**, 409–425.